Ultra-Thin Integrated ALD Alumina Electron-transparent Windows for Nanoreactor Applications

Levar Martin Goossen

Department of Microelectronics

Faculty of Electrical Engineering, Mathematics, and Computer Science

Delft University of Technology

April, 2018

Ultra-Thin Integrated ALD Alumina Electron-transparent Windows for Nanoreactor Applications

by

Levar Martin Goossen

in partial fulfillment of the requirements for the degree of

Master of Science
in Microelectronics

at the Delft University of Technology,
to be defended publicly on Monday April 23, 2018 at 10:00 AM.

Supervisor:	Prof. Dr. P. M. Sarro,	TU Delft
Thesis committee:	Dr. J. Wei,	EKL, TU Delft
	Prof. Dr. M. Mastrangeli,	TU Delft
	Prof. Dr. I. M. N. Groot,	U Leiden

TU Delft Delft University of Technology

EKL Else Kooi Laboratory

To my family,

whom have unconditionally supported me always.

ABSTRACT

Nanocatalysis has received considerable attention in the scientific community due to their superior reactivity compared to their macro-sized counterparts. MEMS nanoreactors allow scientists to view these reactions in-situ. This opens up doors to finally understanding the underlying mechanisms of the nanocatalyst's effectiveness, which may eventually improve our every day lives.

This thesis focuses on the viewing port of the device – the electron-transparent window (ETW) – and how they can be improved for future generations. From scattering theory, it was determined that the best way to improve the imaging quality of current ETWs was to develop thinner ones. Two questions were then asked: can a thinner ETW be integrated into a nanoreactor process? If so, how will it affect the mechanical strength of the ETW?

Aluminum oxide (alumina) was chosen specifically because of its deposition method, atomic layer deposition (ALD). The characteristics and material properties of ALD alumina were assessed and it was determined that they are suitable for ETW applications.

Using ALD alumina presented a few challenges in its integration into nanoreactors, especially the use of vapor hydrogen fluoride. ALD alumina ETWs were able to be successfully integrated into a nanoreactor down to 5 nm thick. The 5 nm alumina ETWs are able to withstand a pressure difference at least 0.75 bar, however they were not able to survive inside a TEM as they disintegrated immediately under the electron beam.

Alumina ETWs that are 10 nm were able to be imaged in a TEM. These windows were tested in a transmission electron microscope (TEM) and scanning electron microscope (SEM) to showcase the improved electron-transparency.

The ultra-thin ALD alumina ETWs can improve the imaging quality of nanoreactors, due to their lower thickness compare to current nanoreactors. The successful release of 5 nm membranes may also be useful for other applications, such as sensors.

ACKNOWLEDGEMENTS

I would like to thank...

Dr. Lina Sarro for giving me a project in the ECTM group. It has been an absolute pleasure working with her and in her group.

Dr. Jia Wei in supporting me in my project. He not only gave me perfect advice, he gave me room to grow. Once I had finished my training run, Jia handed me a batch of wafers, told me 'Good Luck' – and walked away. The sudden realization of responsibility of my own work is a feeling I'll never forget. Through my process I learned to appreciate the space and trust Jia gave me. Thank you, Jia.

Dr. Gregory Pandraud, who always offered to help me, even though he was busy with a million other things.

Jian, who in many occasions helped me in the clean room while I was getting on my feet.

Dr. Huaxi Xie and Dr. Can Duan. Both of them allowed me to take part in their research project as an undergraduate student that sparked my interest in MEMS.

Alexander, Violeta, and Sylvania. Alexander and Violeta for their help with knowledge of the in-and-outs of the ALD machine. Violeta especially, who helped with some extra depositions towards the end. Sylvania for her grace and understanding, as I have made a couple errors while working in the clean room.

My ECTM colleagues, especially my office-mates Joost, Ziqao and Thijs who have always given me company throughout the year. A special thanks to Sarat, who was my partner from day one.

Arturo, Eduardo, Hannah and Sophie, my good friends here in the Netherlands. I'm grateful for those friendships.

Brad and Matt, I don't see how I could've made it out of Florida without you guys.

My girlfriend, Janka, who has always inspired me to become a better person.

Lastly, I would like to thank my family. Emiro, Souad and my parents. They have supported me to no end, and I can't thank them enough.

CONTENTS

LIST OF FIGURES

LIST OF TABLES

1 INTRODUCTION AND MOTIVATION

Nanoreactors are designed to provide the best imaging experience for the transmission electron microscope (TEM) user while simultaneously withstanding the harsh environmental requirements needed to support nano-catalytic reactions. This thesis will explore one component of the nanoreactor – the electron transparent window (ETW), which is the viewing port of the device. Current ETW materials have provided good image quality for thicker and heavier nano-particles (NPs), however imaging issues arise in experiments when lighter NPs are desired.

In this chapter, the driving reasons for the need to study nanocatalysis are discussed in section 1.1. In the following section, the MEMS nanoreactor and components are introduced. In section 1.3 the ETW is further explained, with a list of its requirements. Lastly, the motivation and outline for this thesis are given in section 1.4.

1.1 Nanocatalysis and Their Reactions

Catalysts are chemical molecules that facilitate a chemical reaction by lowering the energy required to complete it. Catalysts are used abundantly in our lives, such as purifying the fuel in our cars and airplanes [1]. While it has been known that reducing a catalyst's size will increase the effectiveness of a catalytic reaction because of the increased surface (and defect) area of the catalyst, it has been discovered that NPs exhibit different reaction mechanisms due to quantum effects of their electronic behaviors [2]. Results of this are a significant reduction in temperature needed for catalytic reactions [3]. Another is the enhancement of oxygen storage capabilities compared to their undoped counterparts [4]. The in-situ (i.e imaging during the reaction) characterizations of these reactions becomes then instrumental in developing a better understanding of these unexplored underlying quantum effects [2].

1.2 MEMS Nanoreactors

The rate of catalytic reactions depend on two things: temperature, to supply the reaction with additional energy; and pressure, to increase the rate of collision between the reactants [5]. Nanoreactors are MEMS (micro electrical-mechanical system) micromachined devices which control the reaction environment during imaging inside a TEM. This is challenging, as TEMs operate in vacuums to allow a collision-free path from the electron gun and the specimen. There are many different forms of nanoreactors which are used to form the environmentally controlled chamber. Temperature is controlled by the integration of metal microheaters (currently molybdenum [5] or platinum [6]) on the nanoreactor which is then biased to generate heat directly on the chip. Pressure is controlled by gas inlets and outlets called microchannels. Microchannels allow the user to input a gas or liquid at a specified pressure and flow.

In the nanoreactor, the ETWs are suspended in a thicker, mechanically supporting membrane, where the microheater is typically integrated. An illustration of the nanoreactor and its components can be seen in figure 1.1. An in-depth overview of a proto-generational and modern MEMS nanoreactors can be read in [7],[8] respectively.

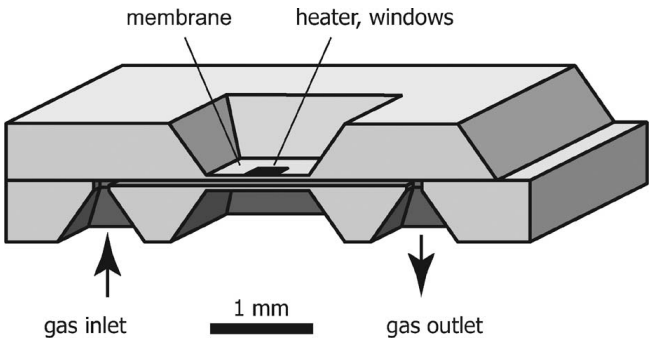

Figure 1.1: An illustration of a MEMS nanoreactor main components labeled. Abstracted from [7], figure 1.

1.3 Electron Transparent Windows and Their Requirements

ETWs are ultra-thin membranes which are the viewing point for the TEM user. By strict definition, ETWs are not transparent but translucent as $T < 1$, where T is the transmission of electrons through the window. Multiple windows are always present in a nanoreactor as there is no direct control of NP deposition on the ETWs. NPs are typically inserted via liquid suspension which spreads the NPs randomly across the whole device. ETWs are usually 1 to 10 μm^2 in area, which is most likely the result of a natural optimization between pressure strength and desired viewing area of a TEM user. Figure 1.2 is an illustration of how TEM imaging of NPs work, to already form some understanding. Materials used in the window have varied over the years. Silicon nitride (SiN) ETWs are currently in production in the Else Kooi laboratory (EKL) [7]; (amorphous silicon) a-Si, (silicon dioxide) SiO_2 and most recently, (amorphous silicon carbide) a-SiC have been also explored [9].

There are many ways to characterize the quality of ETWs as they function in nanoreactors. Nanoreactors are currently used at 1 bar pressure, with the likelihood of requiring higher pressures as nanocatalyic research develops further. Below is a list of requirements for ETWs in nanoreactors examined in this thesis:

- Imaging Quality

  ETWs should be thin to reduce the amount of electrons scattering within it. Thinner membranes allow the path of the electron from gun to specimen to be minimally disturbed, which in turn improves the clarity of the image [chapter 6]. The surface of the ETWs should also be as uniform as possible for a smooth imaging background [section 3.5.2].

- Mechanical Strength

  The window should be durable and pin-hole free to withstand the pressure within the reactor [section 3.4.2, chapter 5]. A rupture in the membrane will ruin the experiment, and can even damage the TEM.

- Environmental Demands

  Electrical Conductivity — This is caused by the electron beam. In this case, the membrane and/or nano-catalysts can become charged by the electrons penetrating the material. This is undesirable as it can cause scattering of the catalysts across

the windows [chapter 6].

Chemical Resistance — The NPs and the carrier mixture can contain chemicals which may attack the windows. This can eventually destroy the device. Chemical resistivity affects the longevity of the device. This is an application based criteria [section 3.8.2].

Beam Resistance — The TEM microscope shoots more than 10^{10} electrons nm^{-2} s^{-1} [9]. This can cause the window to deform and finally puncture it. Beam resistance is measured by the survival time of a window at a given electron beam intensity [9][section 3.7.2, chapter 6].

Wettability — Because the NPs are suspended in a liquid mixture, the wettability of the window is important as it allows for easier positioning of the samples [9][section 3.7.2].

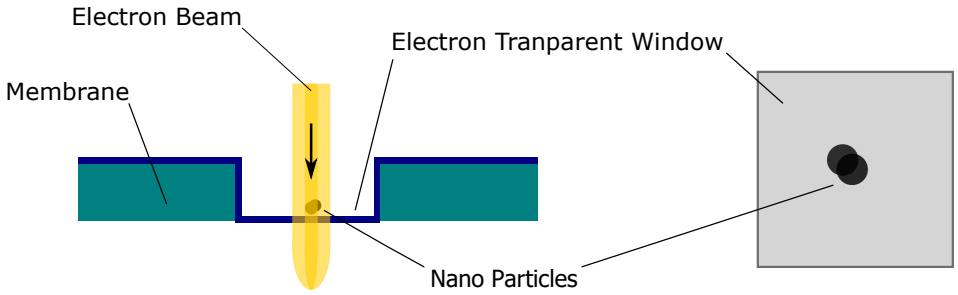

Figure 1.2: A drawing of TEM imaging of NPs on ETWs (left), and the expected result of a TEM image taken (right). The right image is a top-view of the left image.

1.4 Motivation and Thesis Outline

To get a deeper and broader understanding of the workings behind nanocatalysis, nanoreactor ETWs must be made thinner to increase resolution, and thicker to withstand the inevitable demand for higher reaction pressures. Currently, commercially sold nanoreactors have ETWs that are 15 nm thick and can withstand 1 bar [10].

The following research questions to be answered in this thesis:

— Can ultra-thin atomic layer deposited aluminum oxide (ALD Al_2O_3 / alumina) be suitable and better replacement for current ETW materials?

— If so, how will the minute thickness affect the mechanical properties of the ETWs?

In chapter 2, the theory and modeling of how ETW material properties affect a TEM image will be presented and discussed. Next, reasons for selecting ALD Al_2O_3 and its characterization will be described in chapter 3. The integration of alumina into a nanoreactor process will be shown and discussed in chapter 4. Mechanical and imaging experimentation and results will be given in chapter 5 and chapter 6 respectively. Lastly, the conclusion and future suggestions are offered in chapter 7.

2

THEORY AND MODELING OF ELECTRONTRANSPARENCY

The density, atomic number, and thickness of the ETW are all important qualities to capture the best TEM image possible. An introduction to electron imaging will be given in sections 2.1 and 2.2. Scattering terminology will be defined in section 2.3, which will give a foundation before presenting Rutherford's scattering cross section in section 2.4. Modifications of the cross section to improve the model's precision can be found in appendix A.1. Finally, how the film properties affect spatial resolution will be discussed and summarized in section 2.5. Extra information of how properties of the ETW affects contrast in TEM imaging is detailed in appendix A.2.

2.1 Electron Imaging

Like any microscope, the goal is to view samples at a specified magnification. TEMs use electrons as their means of forming images. While visual light microscopes (VLMs) are constrained by the detection limit ($\lambda \approx 390$ nm) of our eyes, TEM microscopes are able to surpass this limit using the wave-like nature of electrons. It was Louis De Broglie in 1924 who discovered this behavior [11]:

$$\lambda = \frac{h}{p} = \frac{h}{m_0 v}\sqrt{1 - \frac{v^2}{c^2}} \tag{2.1}$$

Where h represents the Planck's constant, and m_0, v, and p represent the rest mass, velocity, and momentum of the electron respectively. The applicable takeaway from equation (2.1) is this: the faster we can propel electrons, the smaller its wavelength will be. For example, a 200 keV TEM accelerates electrons to a λ of 2.5 pm. This is the main essence of the TEM microscope, and consequently why they are so large – kilo-volts of suspension are needed to realize pico-scale resolution [12]. The wavelength of an electron or photon is directly related to the angular resolution by the Rayleigh criterion [13]. The angular resolution, δ in meters, is the minimum distance between two points that a microscope can resolve:

$$\delta = \frac{1.22\lambda}{2n \cdot sin\alpha} \tag{2.2}$$

Where n is the refractive index (RI) of the material between the sample and objective lens (vacuum, $\therefore$ n = 1) and α is the acceptance angle of the objective lens of electrons

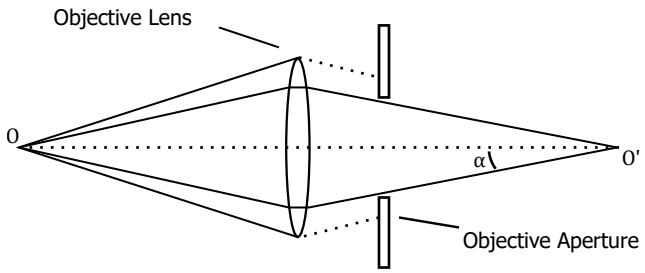

Figure 2.1: The acceptance angle α, is formed by the objective aperture and the objective lens. O is an image which forms an inverted virtual image O' across the objective lens.

scattering from the specimen. The product $n \cdot sin\alpha$ is known also as the numerical aperture (NA). In the TEM, the acceptance angle is deliberately modified by using an objective aperture (figure 2.1). The relationship between the acceleration voltage V and the electron energy is the product of V and q, the elementary charge. The velocity is acquired by creating a magnetic field, recalling the Lorentz force law:

$$F = -q \cdot (E_i + v \times B) \tag{2.3}$$

Where E_i and B represent the electric and magnetic fields respectively and F is the resulting force applied to the electron. Multiple sizable water-cooled electromagnets are powered to create a large electric field, which in turn accelerates the electrons [14]. These electrons need to be accelerated through a vacuum so that they have a collision-free path to the specimen. This is important as it becomes a strict design requirement of the nano-reactor: the electron transparent windows should be durable enough to withstand the pressure differences without rupturing, while also being pinhole-free to contain the pressure.

These electrons are guided through a series of lenses and apertures that add magnification, contrast, and adjust the focus of the image. A lens is an object that can focus and magnify radiation [13]. While optical lenses are made out of glass, electron lenses are magnetic solenoids that use the magnetic fields to alter the path of the electrons [11]. A lens creates a virtual copy on the opposite side of it, this point is called the focal point. The distance between a lens and its focal point is the focal length, f. An aperture is a circular hole of a certain diameter d, which is controlled by increasing (or decreasing) the opening of a diaphragm. The aperture lies on the optical axis. The diameter of the aperture and its position on the focal length determines an acceptance angle α. Electrons deflected at an angle larger than α do not reach the focal point. The relationship between α, f and d is:

$$\alpha \approx tan\alpha = \frac{f}{2d} \tag{2.4}$$

2.2 The TEM Imaging System

Some familiarity with the imaging system of a TEM microscope is useful before moving on to theory. Below is an overview of various imaging components of the TEM, from electron gun to charged coupled device (CCD) camera. In figure 2.2a an illustration of these components can be seen.

- Electron Gun

  The free electrons used for imaging are generated by an electron gun. The beam emitted from the electron gun is usually modeled to have a Gaussian distribution [11]. There are three main types of emission sources used in electron guns: thermionic, field, and Schotty [14].

- The Condenser Lens System

  This system consists of two lenses and an aperture. It is responsible for guiding the electrons emitted from the electron gun onto the specimen. These lenses are named simply condenser 1 (C1) and condenser 2 (C2). This system condenses the electron beam created by the electron gun into a spot size with a certain diameter and intensity, effectively controlling the electron flux passing through this lens system. The spot size and intensity can be manually controlled by the TEM user.

- Specimen Stage

  The specimen plane or stage is where the nanoreactor rests. Because of the magnification capabilities of a TEM microscope, special care is taken to ensure the stability of the holder to reduce motion, which will cause blurring at the nano-scale

level [14]. This becomes especially important when imaging in high resolution TEM (HRTEM).

- Objective Lens System

  This system consists of one lens and aperture. The lens creates the first real image of the specimen, and lies directly below the specimen. Electrons that strike the specimen cause them to scatter and hit the aperture, removing them from the final image. The acceptance angle created by this lens and aperture is directly responsible for the contrast seen in the final image. This will be explained in more detail in the following section.

- Intermediate and Projective Lenses

  The intermediate lens system looks at the first virtual image created by the objective lens. They adjust the focal length gradually, to create even more magnification. There can be multiple intermediates lenses. The projective lens guides the image to the observation screen and it is the last lens the electrons will pass [12].

- Observation Screen

  The observation screen is where the final image is copied. Using a luminescent thin film, the impending electrons leave behind a bright spot, depending on the electron flux at that given point. The local variances of flux create a contrast, forming a live visual image [14].

- CCD Camera

  Once the desired image is in focus, the observation screen is removed such that the electron path directly strikes the CCD. Each pixel will absorb a charge, depending on the electron flux striking it. The amount of charge in each pixel is converted to create a digital image by an analog-to-digital converter (16-bit).

No video? CCD cameras use large capacitors to form their images. The size of the capacitors increases the dynamic range capabilities of the image. The drawbacks however, are longer acquisition times and the inability to capture videos as the frame rate (frequency response) is severely limited by the gigantic RC constants of the camera [11].

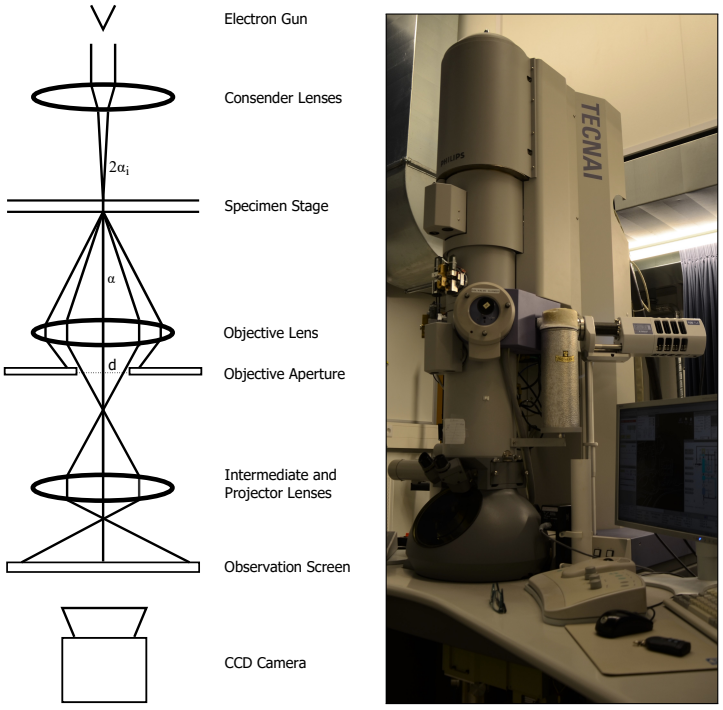

(a) (b)

Figure 2.2: (a) Illustration of TEM components, and (b) a FEI TECNAI 200 keV TEM, at the TNW faculty, TU Delft.

2.3 Electron Scattering

Reducing scattering is essential to form clear NP images in the TEM. The less strongly the ETW scatters electrons, the better the TEM image will be. Scattering is an interaction between two or more particles that cause a change in direction, energy or both. Electrons can be said to scatter elastically (figure 2.3a) or in-elastically (figure 2.3b). Elastic scattering changes the particle's trajectory only, while energy is conserved. Inelastic scattering is when the trajectory and the energies of the particles are changed.

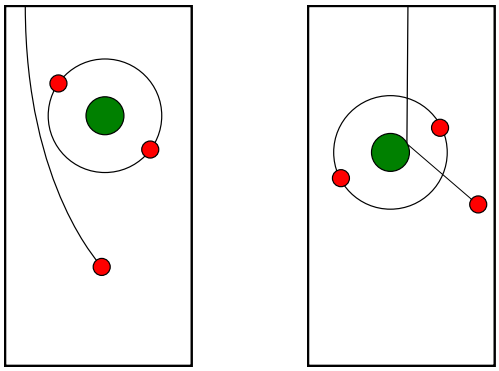

(a) (b)

Figure 2.3: (a) an elastically scattered electron, and (b) an in-elasically scattered electron

A cross section (CS) is seen as an area where an event has a probability of occurring. A quote taken from [11] sums up this concept perfectly:

> "If I throw a ball at a glass window one square foot in area, there may be one chance in ten that the window will break and nine chances in ten that the ball will just bounce. In the physicist's language this particular window, for a ball thrown in this particular way, has a disintegration (inelastic!) cross section of 0.1 square feet and an elastic cross section of 0.9 square feet."
>
> - Rudolf Peierls (Rhodes 1986)

The CS is denoted by Greek letter σ, has units of m^2, and is always dependent on an angle or range of angles. For example, a ball that is thrown perpendicularly from one side of the window and breaks the window, includes scattering angles from 0 to $\pi/2$ radians – whereas a ball that bounces back, includes scattering angles from $\pi/2$ to π radians (figure 2.4). All angles are seen as semi-angles, meaning that angle ranges are mirrored across the angle of incidence and doubled. Although multiple scattering events can occur between an electron and specimen, it is assumed that each event is independent from another so:

$$2\pi \int_0^{\pi} \sigma(\theta)_{obj} sin\theta \cdot d\theta = 1 \tag{2.5}$$

Now it is important to find the probability distribution function (PDF) of a CS from 0 to π. This is called the differential cross section (DSC) with units $\frac{d\sigma}{d\Omega}$. The DSC gives us the probability that an electron will be scattered at angle θ into solid angle Ω.

The trigonometric relationship between Ω and θ (figure 2.5) is:

$$\Omega = 2\pi(1 - cos\theta) \tag{2.6a}$$

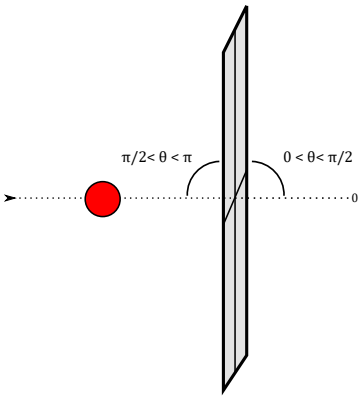

Figure 2.4: Illustration of Rudolf Peierl's quote.

$$d\Omega = 2\pi sin\theta \cdot d\theta \tag{2.6b}$$

and finally putting the DSC together:

$$\frac{d\sigma}{d\Omega} = \frac{1}{2\pi sin\theta}\frac{d\sigma}{d\theta} \tag{2.6c}$$

Now, taking a spherical integral to retrieve the probability of an electron being scattered within a range of angles θ_0 to θ_1 into the prescribed Ω on the inclination angle ϕ:

$$\sigma_{obj} = \int_{\theta_0}^{\theta_1} d\sigma = 2\pi \int_{\theta_0}^{\theta_1} \frac{d\sigma}{d\Omega} sin\theta \cdot d\theta \tag{2.7}$$

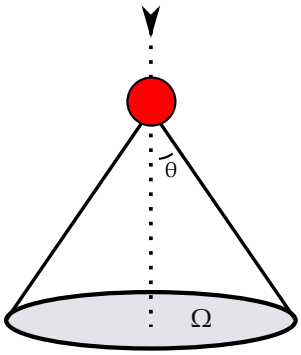

Figure 2.5: Visual representation of the different cross sections and scattering angles.

What if the object is now repeated in a 3-dimensional (3D) film with a density ρ in a volume V? The number density N is defined as the number of atoms per unit volume, atoms m^{-3}:

$$N = \frac{N_a \rho}{A} \tag{2.8}$$

Where N_a is Avogadro's number (mol^{-1}) and A is the atomic mass (u) and density ρ (kg m^{-3}). We can now have the total cross section (TCS) and is defined as:

$$\sigma_t = N \cdot \sigma_{obj} \tag{2.9}$$

Imagine now an electron beam with n electrons. We then modify N from atoms m^{-2} to atoms m^{-3} by multiplying a differential thickness dh. The number of electrons that scatter within the given acceptance angle α can be defined as :

$$\frac{dn}{n} = -\sigma_t(\alpha)dh. \tag{2.10}$$

In nuclear physics cgs units are traditionally used, where $e^2 \rightleftharpoons q^2 \cdot k_0$, and the CS is typically represented as barns = 10^{-24} cm^2 [15].

This is a first order differential equation, which is solved by considering the initial condition $n = n_o$ when $h = 0$, where n_o is the initial number of electrons in the beam, gives:

$$[n]_{\alpha_0}^{\alpha_1}(\rho, Z, h) = n_0 exp(-\sigma_t h) \tag{2.11}$$

where h is the thickness of the film. This relation between transmittance and film thickness is more commonly known as the Beer-Lambert law. One last parameter in scattering theory is the mean free path (MPF), Λ – which has units m^{-1} and is the average length an electron travels before a scattering event occurs.

$$\Lambda = \frac{1}{\sigma_t} \tag{2.12}$$

2.4 Rutherford's Cross Section

Rutherford's CS (σ_R) can readily describe the relationship between material properties of the ETW and how strongly it will scatter the incoming electron beam. Because of the weight difference between electron and nucleus, impeding electrons will change its trajectory due to the interaction with the material's nuclei, while they remain stationary. The trajectory of the electron changes in elastic scattering, the total energy (and therefore the wavelength) is conserved [12][14]. This scattering is caused by Coulomb interaction, which explains the interaction between two electrically charged particles by Coulomb's Law:

$$F_c = k_0 \frac{q_1 q_2}{r^2} \tag{2.13}$$

Where k_0 is Coulomb's constant, q_1 and q_2 represent the charges of two particles, and r the distance between them. The size of the scattering 'area' created by the atom intuitively depends on the amount of positive charge (protons) in the atom.

The following equations are modeled after Rutherford's gold film thin experiment. Rutherford shot positively charged alpha particles ($Z = 2$) onto a couple micrometer thick gold film, then detected the deflection around the film. This experiment, carried out in the early 1900s [16], eventually led to the discovery of the nucleus. This formula will be represented in its DCS and CS forms:

$$\frac{d\sigma}{d\Omega_R} = \left(k_0 \frac{Z \cdot Z' \cdot q^2}{4 \cdot E_o}\right)^2 \frac{1}{sin^4 \frac{\theta}{2}} \tag{2.14a}$$

$$\sigma_R = \left(k_0 \frac{Z \cdot Z' \cdot q^2}{4 \cdot E_0}\right)^2 \frac{1}{tan^2 \frac{\theta}{2}} \tag{2.14b}$$

Where Z is the atomic number of the element, q is the elementary charge, E_0 is the kinetic energy of impending electrons. θ is the angle at which the electron deviates from

its approach. Z' is the atomic number of the incoming particle, since this particle is an electron (Z = 1), it will be left out in future analyses. The functions in equation (2.14) can be visualized in figure 2.6 at $E_0 = 200$ keV.

When dealing with a compound instead of an element the Z becomes a weighted average Z_{eff} [14]:

$$\text{for a compound}: \quad Y_A X_B, \qquad Z_{eff} = \frac{A}{A+B} Z_Y + \frac{B}{A+B} Z_X \tag{2.15}$$

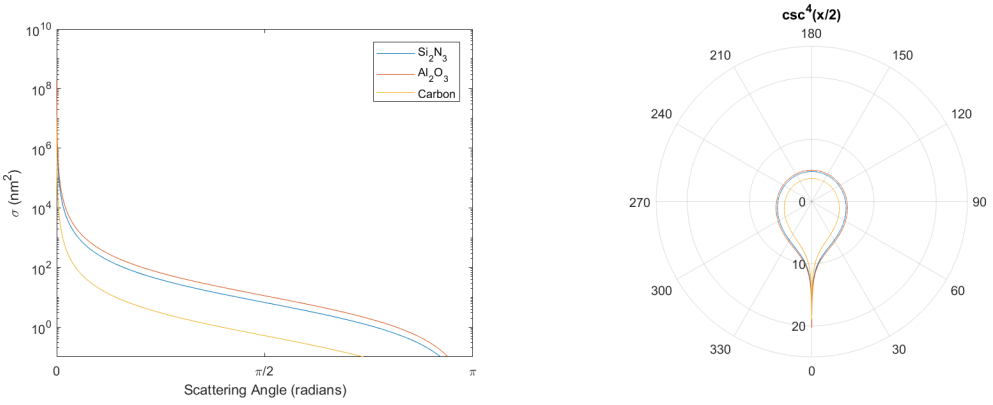

(a) (b)

Figure 2.6: Rutherford's scattering cross section of three different materials. (a) in Cartesian coordinates and (b) in polar coordinates.

The following can be derived from equation (2.14):

- If the film material has a higher atomic number, more scattering will occur – $\propto Z^2$ [equation (2.14)].
- If the film material is denser, more scattering will occur – $\propto \rho$ [equation (2.8)].
- If the film material is thinner, less scattering will occur – $\propto h$ [equation (2.11)].

Looking at equation (2.11), each term also has an exponential dependence on the transmittance, n.

Equation (2.14a) can be broken into two sections: a parametric component and an angular component. The parametric component is a multiplier to the angular component and depends on the material properties of the film. A TEM with an acceleration voltage of 200 keV will have values around 10^{-24} – 10^{-25} m^2. At any given θ, the DSC is proportional to the inverse of E_o^2. Higher electron velocities in the TEM thus reduce the DSC.

A few approximations need to be mentioned. First, this formula ignores other scattering effects and forces – such as in-elastic scattering. In-elastic scattering is ignored because $\sigma_{inelastic}$ is typically around three orders of magnitude smaller than $\sigma_{elastic}$ at TEM energies [12]. Retrieving data from energy-disperse X-ray spectroscopy (EDX) (figure D.3) confirms that inelastic scattering does occur as X-ray emission are a result of electron/atom interaction [17].

Secondly, it is also assumed that only one scattering event can happen to an electron. In other words, an electron has a probability of scattering once or zero times. These

two approximations can be made because of the minute thickness of the film.

Lastly, specimen according to the model do not form diffraction patterns (DPs). DPs are predictable and patterned scattering interference caused by the crystallography of the film material. Even amorphous materials give rise to DPs because while atoms are arranged quasi-randomly in the film, the positioning of an atom and its neighbors are well-defined [11].

2.5 Blurring: Resolution Reduction

Thicker ETWs will reduce image quality. The reason for this is hazing. The less the ETW scatters electrons the less blurring, and the clearer the image will become. Blurring is a result of hazing, however images can also blur by de-focus aberrations or by motion drift [11][13]. Hazing is referred to as beam-spreading in [11]. Beam-spreading describes blurring well, but it is important not to forget that every point inside the beam is being subjected to spreading, not just the circumferential ones. Hazing is well documented in other photonic imaging systems such as magnetic imaging resonance (MRI) and X-ray imaging [18]. Hazing will now be further conceptualized in the spatial and frequency domains:

- Spatial Domain

  Imagine a perfectly circular, uniform and infinitesimally thin-membrane called membrane A. Membrane A is suspended by an infinitely thick square membrane that is imaged by a TEM perfectly (no noise). The expected image is seen in figure 2.7a. Now another thin film, membrane B, is placed underneath or above the membrane A. Membrane B will scatter the image formed by Membrane A (figure 2.7b). The interaction between membranes A and B can be expressed mathematically as a convolution of both of their transmittance functions.

  What if membrane A or B were now to be non-uniform? This would cause further degradation of the image quality because the electrons are now scattered non-uniformly through membrane B. In figure 2.9 a HRTEM image of a 10 nm layer of ALD alumina is seen. The non-uniformity of the film would be undesirably imprinted on the final image.

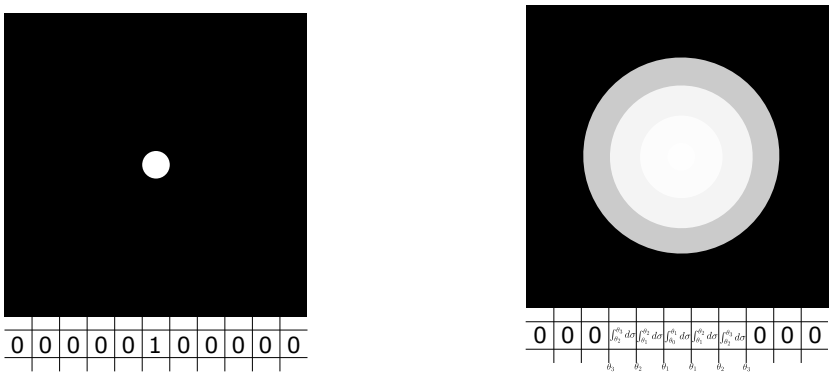

(a) (b)

Figure 2.7: (a) an un-blurred image (Membrane A). (b) a blurred image caused by the beam path also passing a finitely thick membrane (Membrane A and B).

- Frequency Domain

  In the frequency domain, hazing can be described as adding a low-pass filter (LPF) to an image. In figure 2.8 there are two sets of images. In each pair, one is a blurred version of the other. Blurring makes the image more granular, lowering the spectral resolution as sharper contrast differences are filtered out. Following the convolution theorem in the frequency domain, the resulting image is the product of the NP and ETW ones.

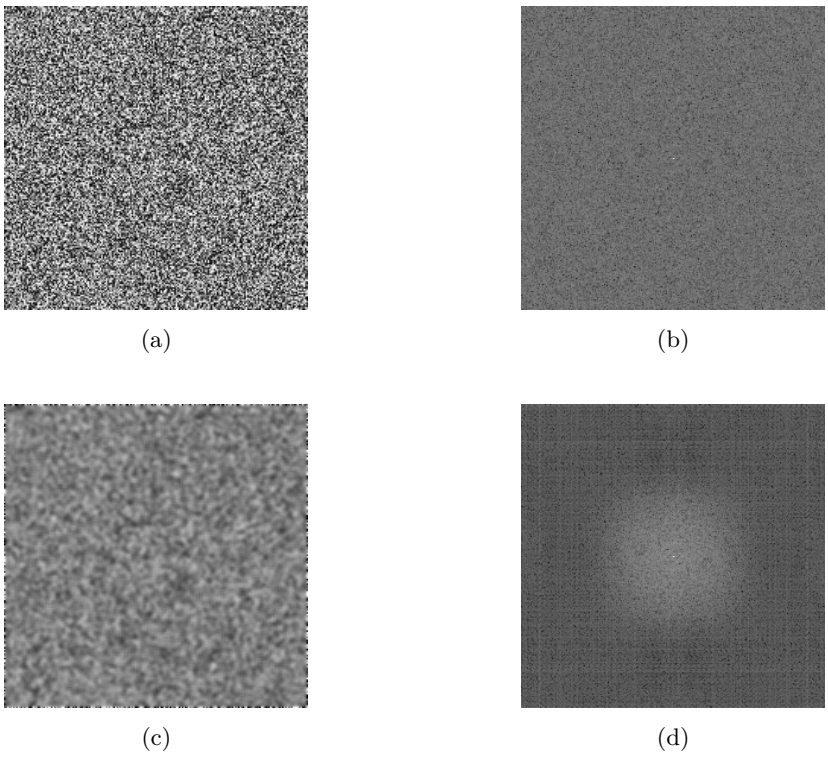

(a) (b)

(c) (d)

Figure 2.8: (a) an image of white noise, with a blurring added (c), and their fast Fourier transform (FFT) of both (b) and (d) respectively.

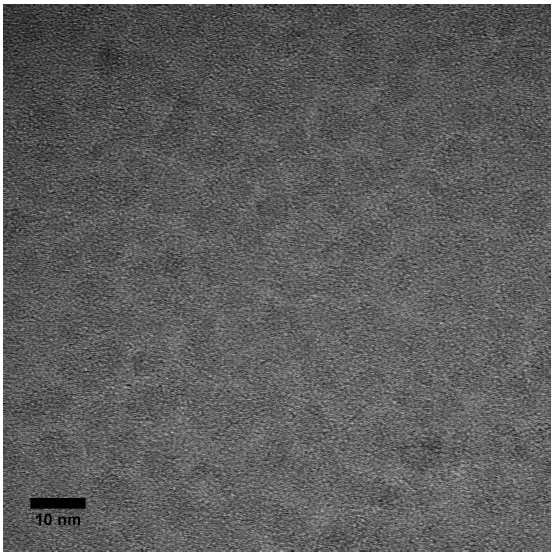

Figure 2.9: TEM image of 10nm alumina window at 450kx magnification.

The digital domain's discrete nature allows the spatial resolution to be easily measured. However, in the analog domain there is no universal approach to quantify it. For example, in [11] full width at tenth maximum (FWTM) is used to quantify the magnitude of hazing. Given $A \approx 2Z$, the relative strength of hazing imposed by the thin material is then:

$$K = exp(\frac{Z\rho}{2} \cdot t) \tag{2.16a}$$

$$K \cdot t = exp(\frac{Z\rho}{2}) \tag{2.16b}$$

where K it the material scattering factor. A higher K means the thin film will cause more blurring relative to materials with lower K values.

2.6 conclusions

It can be said from equation (2.16) that the best materials in terms of imaging for ETW applications are those with low atomic weight, density, and thickness. While it is true that there is a multitude of compounds and elements available, Z_{eff} and ρ of compounds that can be deposited in the EKL do not vary greatly (table 2.1). The most effective way to lower K is to produce the thinnest layer possible. For example, a 5 nm reduction in ETW thickness will result in a 81% reduction in K for the same material.

Table 2.1: Z_{eff} and ρ of various materials available in the EKL. Data taken from (SiN, [19]; Al_2O_3, [20]; SiC [9]).

	Z_{eff}	ρ (g cm^{-3})
LPCVD SiN	10	2.8
ALD Al_2O_3	10	3.1
LPCVD SiC	9.2	2.7

3

DEPOSITION AND CHARACTERIZATION OF ALD ALUMINA

In this chapter, various characteristics of ALD alumina will be measured and analyzed. The reasoning behind selecting ALD alumina as an ETW material will be discussed in section 3.1. Information about the growth of ALD alumina is given in section 3.2. Various material properties of ALD alumina are evaluated throughout sections 3.3 to 3.8, ending with a conclusion in section 3.9.

3.1 Why Atomic Layer Deposition Alumina

Low pressure chemical vapor deposition (LPCVD) is known for its fantastic step coverage and uniformity that can be as low as 0.3 nm-RMS roughness [21]. While it is possible to grow ultra-thin, pin-hole free layers with LPCVD with certain precursors and temperatures [22], LPCVD materials that could be deposited in the EKL - SiN and SiC - retain their good qualities only down to ∼15 nm [9]. Therefore the deposition technique from ALD is needed, which can retain the good properties of LPCVD at even lower thicknesses. In the EKL the only ALD material currently available is alumina. This is why alumina, in particular, was chosen to replace ETWs integrated into nanoreactors in this thesis.

3.2 Atomic Layer Deposition of Alumina

There has been extensive research in ETWs composed of SiN and SiC [9][23]. Both materials are deposited via LPCVD amorphously. A layer that is 15 nm thick made of SiN and SiC are able to withstand at least 1 bar [9][10]. ALD on the other hand, possesses not only better uniformity than LPCVD, it was also found to give pin-hole free layers down to 5 nm – and perhaps even thinner.

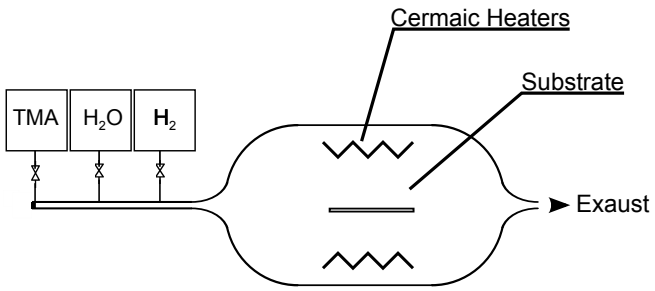

Figure 3.1: A Simplified illustration of the ALD reaction chamber.

Both LPCVD and ALD use two (or more) precursor gasses to form the deposited layer. ALD pulses each precursor one at a time into the reaction chamber. An overview of the reaction chamber and gasses is depicted in figure 3.1. Before the next precursor enters the chamber, the gas and the byproducts are completely purged out of the

chamber. This is done by using inert nitrogen (N_2) gas. The injection and purging of both precursors is known as a cycle. The precursor and purge timings were 1 s and 6 s respectively. The precursor gasses in ALD are more reactive compared to LPCVD thus lower thermal energy is required to create the necessary reactions for the deposition [24]. While there is a multitude of precursor combinations available, in this thesis the precursor gasses used were trimethyl-aluminum ($Al(CH_3)_3$ / TMA) and water (H_2O) [25]. In figure 3.2 and equation (3.1) the reaction sequence can be seen.

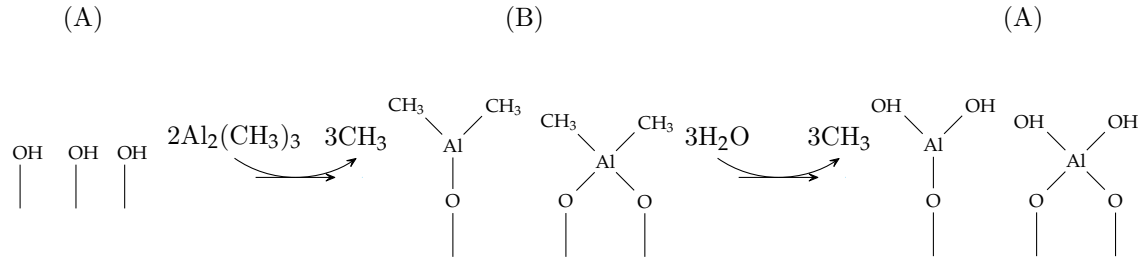

Figure 3.2: One complete cycle of ALD alumina Synthesis [26].

$$\text{(A)} \quad \text{AlOH(s)} + \text{Al(CH}_3\text{)}_3\text{(g)} \longrightarrow \text{Al-O-Al(CH}_3\text{)}_3\text{(s)} + \text{CH}_4\text{(g)} \tag{3.1a}$$

$$\text{(B)} \quad \text{Al(CH}_3\text{)}_3\text{(s)} + \text{H}_2\text{O(g)} \longrightarrow \text{AlOH(s)} + \text{CH}_4\text{(g)} \tag{3.1b}$$

The most important quality of ALD is that it is a self-limiting process. This means that when each precursor is passed into the reaction chamber there is a point of saturation, where all possible reactions between the precursors and substrate have been completed. It is for this reason that ALD is currently the best deposition method for ultra-thin and uniform growth [27]. Notice how the reaction in figure 3.2 begins on hydroxy (-OH) terminated groups. -OH terminated groups can be found on any oxide, varying in -OH group surface concentrations depending on the oxide and deposition parameters [28][29]. While ALD is self-limiting, less than one monolayer is grown per cycle. Due to the surface free energy (γ) of the substrate, the surface species and/or ligand (CH_3 group) may desorb. Free energy in the system decreases with increasing temperature (Gibbs free energy). The growth per cycle (GPC - in Å cycle^{-1}) then is dependent on the stability of the surface species and ligands (-CH_3, -OH) which is dependent on temperature. At higher temperatures, the surface free energy can be reduced by the rearrangement of surface species [26]. There are other growing phenomena that have not been mentioned, as the GPC tends to decrease again after 250-300°C, partly due to increased ligand desorption rates [24][30]. Other considerable temperature dependent effects include: density [31][32], stress [30], refraction index [30][32], electrical properties [31], and elemental composition [32] of the film.

3.3 Growth Rate and Thickness

The thickness of the ETW layer is a parameter needed for most experiments and analyses in this thesis. The GPC indicates how accurately this ALD system can reliably deposit thicknesses at different cycle counts.

3.3.1 Procedure

Alumina was deposited with an ASM F-120. The thickness was measured using a J.A. WOOLLAM XLS-100. The WOOLLAM is an ellipsometer, which measures the change

in light polarization after reflection off the wafer. The change in polarization is dependent on the material properties and thickness, and wavelength of the emitted light [33]. A model can then be created to fit known materials to unknown thicknesses. A stack of multiple materials can be modeled accurately if the previous layer thickness was measured and used as a constant for the model. For example: for this test the alumina was grown on thermal silica, so the silica must be measured first. All measurements made with the WOOLLAM were 9-point measurements. After the alumina deposition, another 9-point measurement was made. The model is fitted with both alumina and silica materials, but now with the known thicknesses of the previously measured silica.

There are two reasons why alumina was grown on thermal silica. First, this is to mimic the process in chapter 4. Second, by growing and measuring thermal silica, it is possible to circumvent the unknown thickness of native oxide present. This allows a more precise model to be made when measuring the ultra-thin alumina. The ASM was first profiled to 20 nm. Assuming that ALD deposits linearly with the number of cycles, the cycle number for the 15 nm, 10 nm and 5 nm targets were established.

Silicon is known to form 2-10 Å of native oxide on its surface [34].

Prior to ALD, the wafers were always cleaned in a 10 min bath in nitric acid (HNO_3) at room temperature, followed by a 5 min de-ionized water rinse (DI-Rinse), followed by HNO_3 at 85°C, followed again by a 5 min DI-Rinse. It is unknown how HNO_3 affects the surface of the thermal silica, and more particularly the -OH group concentration.

Because of the small area (0.1 mm^2) of the windows, it was impossible to measure the alumina thickness on the process wafers, as the ellipsometer scans a large area of around 3 mm^2. The ASM F-120 machine does allow for two wafers to be loaded at the same time, however the measured alumina thicknesses on both wafers varied by around 2 nm, thus all of the tested wafers were loaded only one at a time.

3.3.2 Results

The GPC calculated at 300°C is 0.8 Å $cycle^{-1}$. This result is 0.2 lower compared to [31] and 0.1 lower compared to [35]. Both were calculated from a linear fit with a similar cycle count (= 200, 300), and using the same deposition temperature and precursors. However, different deposition systems and substrates were used in those works. In figure 3.3 the thickness vs. cycle number is displayed. Table 3.1 shows the thickness and relative standard deviation (RSD)[1]. All thicknesses were under 10% RSD, which indicates good repeatably in ALD.

Number of Cycles	Avg Thickness (nm)	RSD (%)
50	4.83	7.48
115	9.81	2.19
180	15.19	2.76
245	20.28	2.97

Table 3.1: Number of cycles vs. thickness used in the process.

1 RSD = $\frac{SD}{Average}100\%$

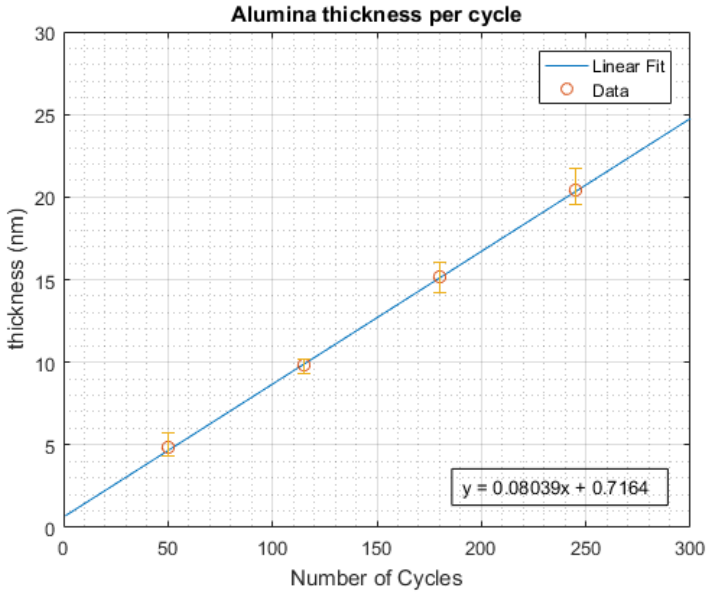

Figure 3.3: Thickness per cycle of ALD alumina 300°C. The data is fitted linearly.

3.4 Layer Continuity

Layer continuity is necessary as the ETWs act as a mechanical barrier which contains the environment inside the nanoreactor from the TEM vacuum.

3.4.1 Procedure

The pin-hole density was tested by etching ALD alumina deposited on a silicon wafer, with 200 nm of thermal silica grown on it, in VHF. Because VHF etches silica and not alumina, discoloration on the wafer due to silica removal can visibly show if pin-holes existed.

3.4.2 Results

ALD alumina was found to be pin-hole free up to 5 nm. Discoloration of the wafer happens only around the edges. This could indicate that handling of the wafer with manual tweezers can damage and open 5 nm thick alumina layer.

3.5 Surface Uniformity

Mentioned towards the end of section 2.5, it is desirable to have a uniform ETW for a smooth backdrop to image the NPs on. Surface uniformity of ALD alumina is a fairly stable parameter; it does not depend greatly on deposition temperature [32] or the number of cycles grown [36].

3.5.1 Procedure

The surface roughness was measured using an atomic force microscope (AFM). The AFM makes use of a micro-machined cantilever with a fine tip attached to it. This AFM measurement was configured in 'tapping mode', where the cantilever is oscillated near its resonance frequency. The resonance frequency of the cantilever used for this measurement was between 140-390 kHz. The change in height is measured by a laser

that is beamed at the tip of the cantilever and reflected back to a photo-detector, while raster-scanning a specified area. The detector measures the change in frequency of the cantilever, which is dependent on the height of the substrate surface. Surface uniformity is standardly measured in root mean squared (RMS)[2].

3.5.2 Results

The RMS roughness (S_q in Å) of a 5 nm ALD layer was 4.0 (figure 3.4), which is a smooth layer considering the small thickness. A 30 nm thick layer of ALD alumina was measured to have a S_q of 3.0 [38], which indicates a minor decrease in S_q with increasing thickness. For comparison, a 40 nm LPCVD SiC with gas flow rate (GFR = 2) has a S_q of 2.4 [9] which betters both alumina measurements, although at a higher thickness.

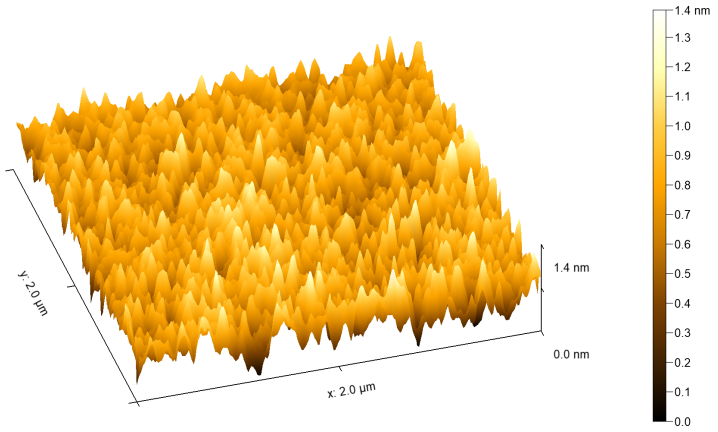

Figure 3.4: A 3D reconstruction of an AFM scan on a 5 nm thick alumina film deposited on 300 nm of thermal silica.

3.6 Residual Stress

Residual stress is a property that is especially important for thin-film membranes as it determines the amount of bulging or tautness of the released film. Stress is introduced to thin films in various ways. The total residual stress (Σ_{res}) is a summation of intrinsic (Σ_{int}) and thermal stress (Σ_{th}),

$$\Sigma_{res} = \Sigma_{int} + \Sigma_{th} \tag{3.2}$$

Σ_{int} is caused by the growth of the thin-film. There are many different ways films can nucleate, grow, and coalesce on substrates. ALD Σ_{int} is therefore a consequence of recipe parameters such as cycle/purge timing, precursor selection, and deposition temperature. The colder the deposition temperature the more tensile Σ_{int} will become [39][40][41]. Σ_{th} on the other hand, is added from the difference in coefficient of thermal expansion (CTE in T^{-1}) and lattice constant between the thin film and the substrate it is grown on [41][42][19]. The relation between Σ_{th} and the CTE of the film and substrate material is given below [41]:

$$\Sigma_{th} = \frac{E_f}{1 - v_f}(\xi_f - \xi_s) \cdot (T_{ALD} - T_{amb}) \tag{3.3}$$

2 $\sqrt{\frac{1}{L}\int_0^L |Z(x)|\,dx}$ where $Z(x)$ is the height profile, x is position, and L is the length [37].

Where E, v_f and ξ denote the Young's modulus, Poisson's ratio and CTE respectively. Subscripts f and s denote if the property belongs to the film or substrate. T_{ALD} and T_{amb} are the deposition temperature and ambient temperature respectively.

Stress is measured in pascals (Pa) and is defined in N m^{-2}. Stress can either be tensile (+Σ) or compressive (-Σ), which either exerts a force inward or outward force in the lateral direction respectively. Depending on the stress, the curvature of the wafer is altered (figure 3.5).

Because the underlying substrate is removed from a now-released membrane, it will relax by tightening (tensile) or buckling (compressive). If the stress exceeds the fracture limit, tensile free standing membranes will tear [43][44][45]. With this knowledge, it can be said that compressive materials are better suited for ultra-thin membranes. While tensile membranes are generally desired as they form flat surfaces upon release, the increase of Σ_{res} with smaller thicknesses might make the membranes more susceptible to tearing during release. There is no risk of tearing in releasing ultra-compressed membranes. The bulging will anyways disappear when pressure is applied within the nanoreactor.

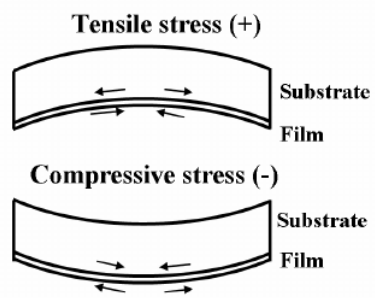

Figure 3.5: Comparison of tensile and compressive stress. Adapted from [46].

3.6.1 Procedure

The stress of the alumina was measured using a TOHO FLX 2320-R. The TOHO measures the radius of the wafer before and after thin-film depositions to determine the amount of stress added to the wafer. The TOHO uses Stoney's equation to measure the stress:

$$\Sigma_f = \frac{E_s h_s^2}{6h_f(1-v_s)}\left(\frac{1}{R}-\frac{1}{R_0}\right) \tag{3.4}$$

Where h_s and h_f are the thickness of the substrate and deposited film respectively, R_0 and R is the radius measured prior and after thin film depositions. Stoney's equation assumes the substrate and films are uniform, isotropic, and linearly elastic [47].

Similar to thickness measurements in section 3.3.1, the alumina layer was deposited on 200 nm of thermal silica. A number of steps were taken to prepare the measurement wafers. The curvature and thickness were measured for the bare silicon wafer and again after the deposition of both silica and alumina. The silicon wafer thickness was measured from a 17-point average by an EICHHORN + HAUSMANN MX 203-6-33. The silica and alumina thicknesses were both measured by the WOOLLAM and are a result of a 9-point average. The TOHO requires the inputs of the substrate and film thicknesses for stress calculations in equation (3.4). Before re-measurements, the front side of the

In calculations the substrate is still the silicon wafer, even though the alumina is deposited on thermal oxide.

wafer is covered by photoresist and dipped Buffered HF 1:7 (BHF) until the silica or alumina on the backside is completely removed. The wafer will have to be ashed prior to its re-measurement. These steps are taken to ensure that the wafer remains bare on the backside as it should not contribute to any bending of the wafer. The wafer was measured nine times then averaged in the 0° orientation.

3.6.2 Results

The results of the stress measurements are graphed and tabulated in figure 3.6 and table 3.2. The deposition temperature was at 300°C, which was compressive in the range of thicknesses grown. $|\Sigma_{res}|$ becomes exceedingly high at ultra-thin thicknesses, meaning that the mechanical characteristics can differ greatly from their bulk counterparts. The Young's modulus, which depends on stress, is an important criterion in determining the amount of pressure a membrane can withstand before rupturing.

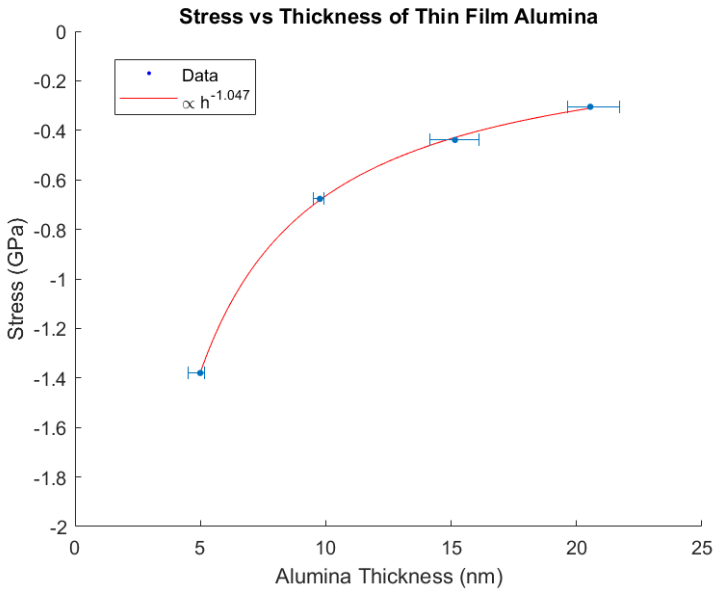

Figure 3.6: Thickness per cycle of ALD alumina at 300°C.

Average Thickness (nm)	Average Stress (GPa)
4.995	-1.378
9.811	-0.681
15.154	-0.442
20.548	-0.305

Table 3.2: Number of cycles vs. thickness used in the process.

3.7 Surface Free Energy

Surface free energy (γ) in mJ m^{-2} is directly related to the wettability [48], sintering [49] properties and beam resistance [9] of a material. Surface free energy can be thought

of as the energy required to cut the material in half.

Wettability — NPs are currently loaded onto nanoreactors by liquid suspension, therefore a certain amount of wettability is needed to reliably settle NPs on the ETWs. For example: in [1], water is used to deposit NPs. A surface is described as either hydrophilic or -phobic, which is measured by the contact angle a water droplet on its surface [48]. Higher γ increases the wettability of the material. Ethanol (EtOH) or isopropanol (2-propOH) can also substitute water, as they have different wetting properties.

Sintering — At high temperatures NPs on the surface of materials have a tendency to sinter, or migrate towards each other forming larger particles. This is undesirable as it increases the surface area of the NPs during the experiment, retarding the reaction. For example, oxidation of NPs will increase its wetting behavior during the experiment, which can more effortlessly coalesce NPs together [49][50]. A reduction of an ETW's γ can impede NP sintering behaviors by reducing wetting behavior on its surface.

Electron Beam Resistance — During TEM imaging, the high electron beam energies and flux will cause the windows to break [9]. The reason for this is the displacement of atoms due to inelastic collisions with electrons [51]. Materials that are more resistant to electron beams have higher γ because their chemical bonds containing the atom in formation are stronger [9].

3.7.1 Procedure

Only wettability with water will be directly measured in this thesis. Wettability was measured using the sessile drop technique, using a DATAPHYSICS SCA-20. A 7 μL droplet of water is dispensed on a wafer's surface and the contact angle θ_c was measured between the surface and liquid-air interface (figure 3.7). Droplets were deposited five times in five different locations on a silicon wafer with 5 nm ALD alumina layer deposited on it. The angles were measured then averaged.

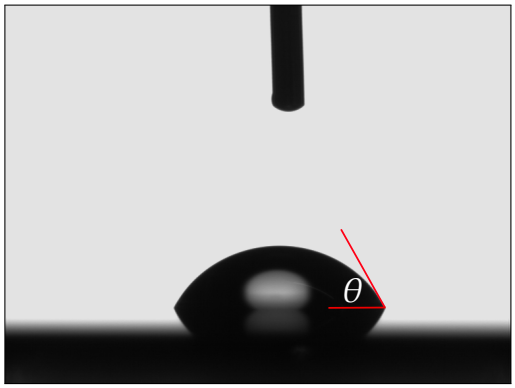

Figure 3.7: A water droplet on an alumina layer. Image taken from a DATAPHYSICS SCA-20.

3.7.2 Results

The γ of ALD alumina is between 38.3-44.9 mJ m^{-2} [38]. The average contact angle was 58.3 degrees, meaning the surface is hydrophilic. There is certainly a trade-off between wettability and sintering-quenching. Sintering is also related to the mismatch between γ of the alumina film and the NP. Sintering-quenching is therefore an application based criteria, which depends on the NPs a TEM user is working with, and also how they intend to use the NPs within a nanoreactor.

3.8 Chemical Inertness

The chemical inertness of the ETW is also an application-specific parameter. It depends on which gasses/liquids the TEM user will be using as reactants for their MEMS nanoreactor experiments. Degradation of the ETW contaminates the experiment by introducing undesirable products into the reaction chamber. Moreover, the ETW can weaken and rupture due to the chemical abrasion. The reactants currently used by TEM users include ambient air, carbon monoxide (CO) and water [1][52]. These reactants are generally used to view the oxidation behavior of the NPs, which poses no threat to alumina – even at high temperatures. As with any emerging technology, it is uncertain what the demands for future applications will be. Therefore, various acids and bases typically used in MEMS processing will be tested. While these chemicals may never be used as reactions for in-situ experiments, they will at least give an overview of etching compatibles for future MEMS processes while also giving insight into its chemical inertness.

It is important to always consider how the high temperatures (currently up to 1000°C) can affect the chemical resistance of the ETWs.

3.8.1 Procedure

The etch rate alumina for alumina was measured in several acids and one base. A single measurement was made with the WOOLLAM before and after the etching. The etch rate of alumina in potassium hydroxide (KOH) was found in table IV in reference [53]. While the reference does not use ALD alumina, the evaporated alumina used in that work has a similar RI to amorphous ALD alumina found in [30] (1.66 and 1.63 respectively) so it will at least give a reasonable approximation of the etch rate. More process-specific etch rates can be found at appendix C.

3.8.2 Results

From table 3.3 it can be seen that SiC is most resistant to multiple clean room etchants, whereas alumina is least resistant.

Table 3.3: The etch rates of ALD Al_2O_3, LPCVD SiN, and LPCVD SiC in various MEMS processing etchants. All etch rates are in nm/minute. All SiC and SiN etch rates were taken from [9] and the EKL respectively.

Etchant	ALD Al_2O_3	LPCVD SiC [a]	LPCVD SiN
BHF 7:1	81.0	1.8×10^{-3}	0.3
0.55% HF	17.4	0	0.2
VHF/EtOH	0	0	3.0 [b]
80% H_3PO_4 at 157°C	40.1	4.8×10^{-3}	25.3
25% KOH at 85°C	>800 [c]	0.3	0.3×10^{-3}

a From [9]
b From [54]
c From [53]

3.9 Conclusions

ALD alumina is an exceptional layer for ETWs with better or similar qualities than LPCVD materials thanks to its low surface roughness, surface continuity, and finely controllable deposition rate. The compressive residual stress of ALD makes it more suitable for the membrane release of ultra-thin layers. However, for harsher chemical environments, LPCVD SiC would be a more suitable option. Because of alumina's weakness in etching solutions, to integrate it into a nanoreactor special steps are needed. This will be explained in the following chapter.

4

INTEGRATION OF ALD ALUMINA IN A NANOREACTOR

In this chapter ALD alumina integrated nanoreactor is processed and analyzed. The nanoreactor geometries and layout are presented in section 4.1. In sections 4.2 to 4.3 the process is described and imaged. Notable and interesting effects of ALD integration are discussed in sections 4.4 to 4.5. Lastly, process improvements and conclusions are given in section 4.6.

4.1 Device Layout and Geometries

The ETWs are integrated in a 800 μm^2 square (figure 4.2c), which is defined by a tetramethylammonium hydroxide (TMAH) etching window from the back side (dotted square in figure 4.1). On the square there are 26, 20 $\times$ 5 μm elongated circles. The circles are patterned in a spiral, in the center of the square membrane. In figure 4.2a an L-edit image of the mask design is displayed. To simplify the process, this thesis does not include the typically integrated microheaters (figure 4.2b). Also not included are the metal traces from the microheater to contacts pad. Figure 4.2d shows an overall image of the device, where each chip is 10 $\times$ 3.3 mm rectangle. The device can be diced towards the end of the process to suit the needs of the TEM user.

In this thesis, only half of the nanoreactor was processed and tested. In reality, two chips seen in figure 4.1 are combined with an O-ring, with the inclusion of microheaters/channels, to form a complete nanoreactor similar to figure 1.1.

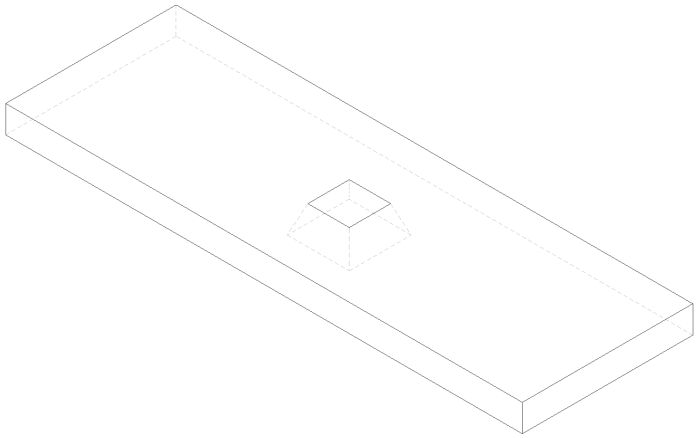

Figure 4.1: A 3D image of the idealized nanoreactor chip. The dotted window underneath it will be etched by TMAH to eventually create a suspended membrane see in figure 4.2c.

4.2 Device Fabrication

The alumina ETWs were created using 3 masks in total. The starting wafers were p-type, 525 mm thick with (100) crystal orientation. There were a few challenges in creating

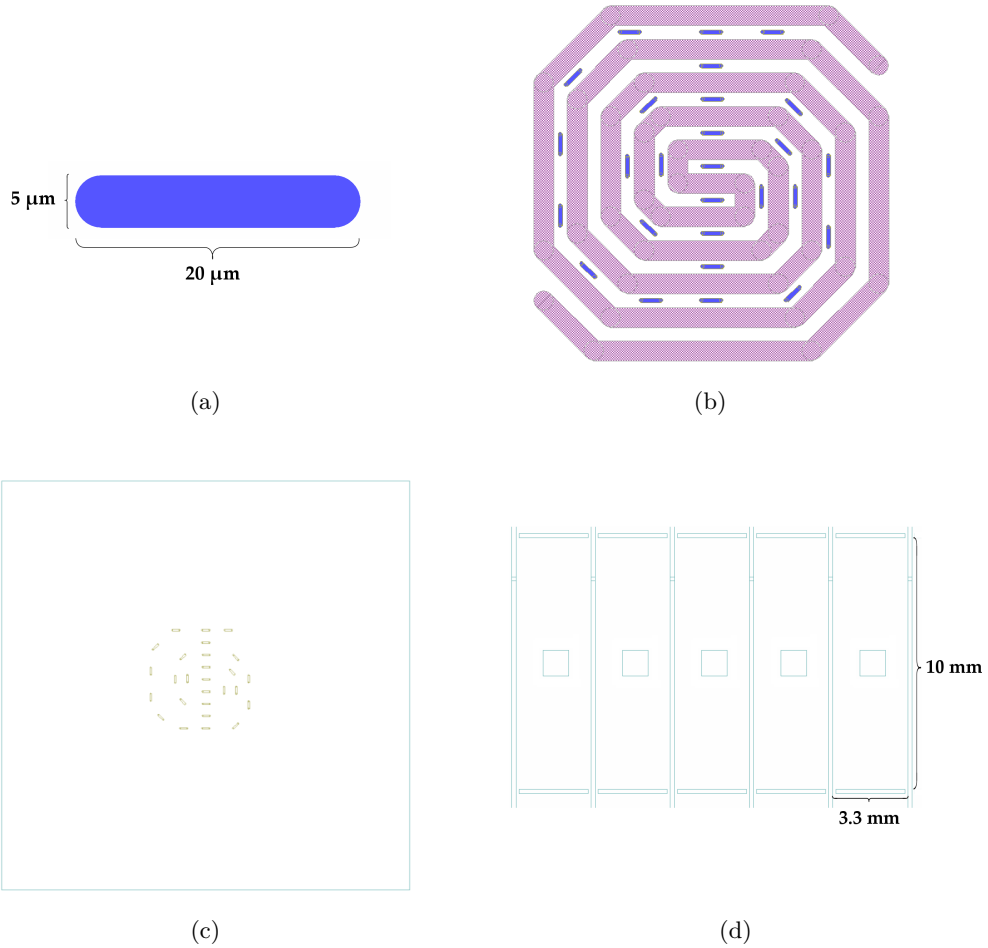

(a) (b)

(c) (d)

Figure 4.2: (a) dimensions of the ETW in this thesis, (b) layout of the ETWs with the normally-included microheater. (c) layout of ETWs spiral inside the 800 μm^2 square, (d) layout of aforementioned square in the die. In the mask design there are 40 die, distributed in 4 rows of 10 die each. All images were taken in L-edit.

the process. Alumina is etched in TMAH, which meant that the ALD alumina had to be deposited on a sacrificial layer resistant to TMAH. The sacrificial layer must at the same time be etched in vapor hydrogen fluoride (VHF), to release the membrane. Thermal silica was chosen as the sacrificial layer as it satisfied both requirements; resistance in TMAH and the lack thereof in VHF. Thermal silica is also a smooth layer, which allows for a more-uniform deposition of the ALD alumina. After ALD, the layer has to be protected (capped) to prevent damage and contamination from further processing. Plasma enhanced chemical vapor deposition of tetraethyl orthosilicate (PECVD TEOS) is used in this process, because it can be etched in VHF but also has a low deposition temperature which keeps the thermal budget small. Realistically, many capping materials can be used.

The complete process is outlined below in nine steps with its visual counterpart in figure 4.3:

a) 200 nm of thermal silica is grown on the silicon wafer. The oxidation temperature was 1000°C [1].The oxide is used as an etchant-stop for the TMAH etch later in the process, and is used as a sacrificial layer at the end of the process.

1 All thermal SiO_2 in this thesis is grown at 1000°C

b) 1 μm of SiN is deposited using LPCVD. The SiN will become the mechanically supporting membrane of the ETWs.

c) On the front-side, the ETW holes were dry-etched to land on the thermal silica.

d) The wafers are etched in BHF to remove the remaining oxide in window holes.

e) 800 nm of thermal oxide is regrown in the window holes. The idea behind process steps d) and e) was to provide a uniform surface for the ALD Al_2O_3 to grow on. The dry etching step done in step c) causes the previous thermal oxide layer to become uneven due to the ion bombardment.

f) Al_2O_3 is deposited via ALD at 300°C.

g) 1 μm of PECVD TEOS is deposited on top of the Al_2O_3. TEOS was chosen as a protective layer for two reasons: because it is a silica, and the deposition is performed at 350°C. Because TEOS is an oxide, it can be removed with VHF simultaneously with the thermal oxide beneath the window in step a). 1 μm was chosen because the selectivity between TEOS and thermal silica was found to be approximately 4.5:1 in VHF. The idea here was that the release of the window from the oxides would occur about the same time. The low deposition temperature of the PECVD also fits the low thermal budget of this process.

h) On the back-side, the TMAH openings are dry-etched to remove the silicon nitride, silicon oxide and alumina to reveal the bare silicon. A 25% TMAH solution at 85°C (with magnetic stirrer) etches the silicon wafer. Prior to the etch the wafer is dipped in 0.55% hydrogen fluoride (HF) for 4 minutes to remove the native oxide present on the exposed silicon. The front side of the wafer needs to be protected in the bath because TEOS etches in TMAH. This was done using a mechanical holder.

i) Lastly, VHF is used to release TEOS and thermal oxide. The wafer was diced before loading into the VHF machine. This was to set controls during the experimental phase of the process.

4.3 System Layout

Various images of the resulting device are depicted in figure 4.4. In figure 4.4a a few particles can be seen laying on a 5 nm alumina ETW, proving that it exists. By looking at the cliff where the supporting membrane ends, it can be seen that the line is not straight but has a wave-like characteristic. This is unwanted as it will reduce the threshold pressure of the ETWs. The smoothness of the surrounding area proves that the film is continuous, as there are no signs of etching of the SiN layer. Additionally, alumina can grow on SiN despite it lacking -OH groups.

4.4 Vapor HF

The alumina windows were released in VHF with the STPS TECHNOLOGIES uEtch. VHF is chosen as the release-etchant for two main reasons. First, VHF has perfect selectivity between alumina and oxides. The VHF etching parameters were 125 Torr with a 190 and 210 sccm of HF and EtOH respectively. Second, rinsing and drying is not needed to remove the etchant from the devices. In general, VHF is a suitable etchant for MEMS devices because the reactants and products can be kept in the gaseous phase, meaning stiction issues are virtually sidestepped [55].

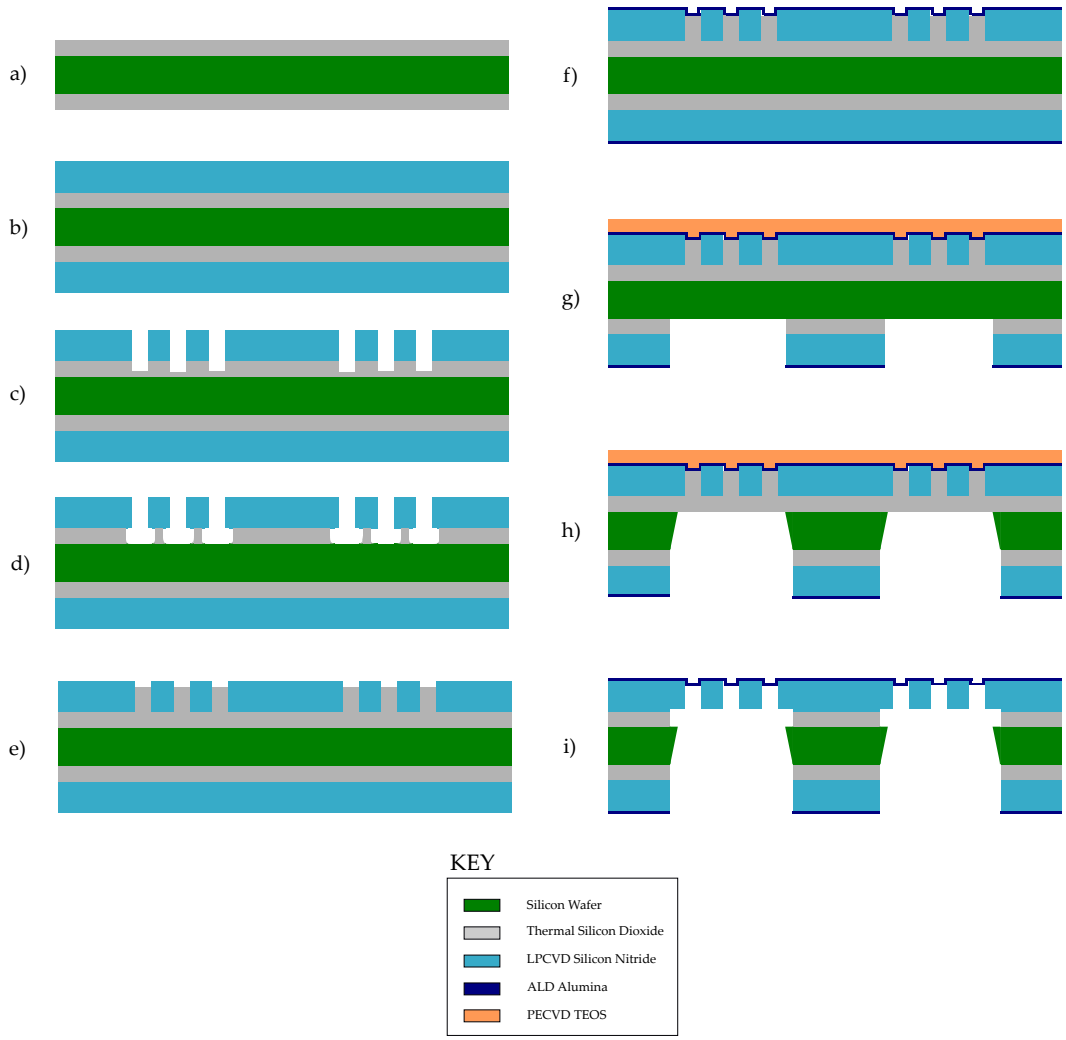

Figure 4.3: Process for the Al_2O_3 ETWs outlined in steps a though i.

The reaction is as follows:

$$SiO_2\,(s) + 4\,HF_2\,(g) \xrightarrow{EtOH} SiF_4\,(g) + 2\,H_2O\,(g) \tag{4.1}$$

EtOH is used here as a catalyst. VHF systems exist without using EtOH but instead use H_2O as a catalyst [56], which is a product in equation (4.1). The H_2O can then in turn be used as a catalyst to further aid the reaction:

$$SiO_2\,(s) + 4\,HF_2\,(g) \xrightarrow{H2O} SiF_4\,(g) + 2\,H_2O\,(g) \tag{4.2}$$

The SPTS preforms etching in cycles, where a purging is performed at the end of every cycle to remove water vapor from the chamber. The etch rate of the SPTS is therefore heavily dependent on cycling times. The pumping down of the reaction chamber allows the water to be kept in its gaseous form [57]. The temperature during the reaction is unknown, however the teflon wafer holder feels warm to the touch directly after etching.

Unlike wet etching, the etch rate of VHF was dependent on how many samples were loaded into the reaction chamber, with more samples reducing the etching rate of the TEOS. This observation was also corroborated in [56].

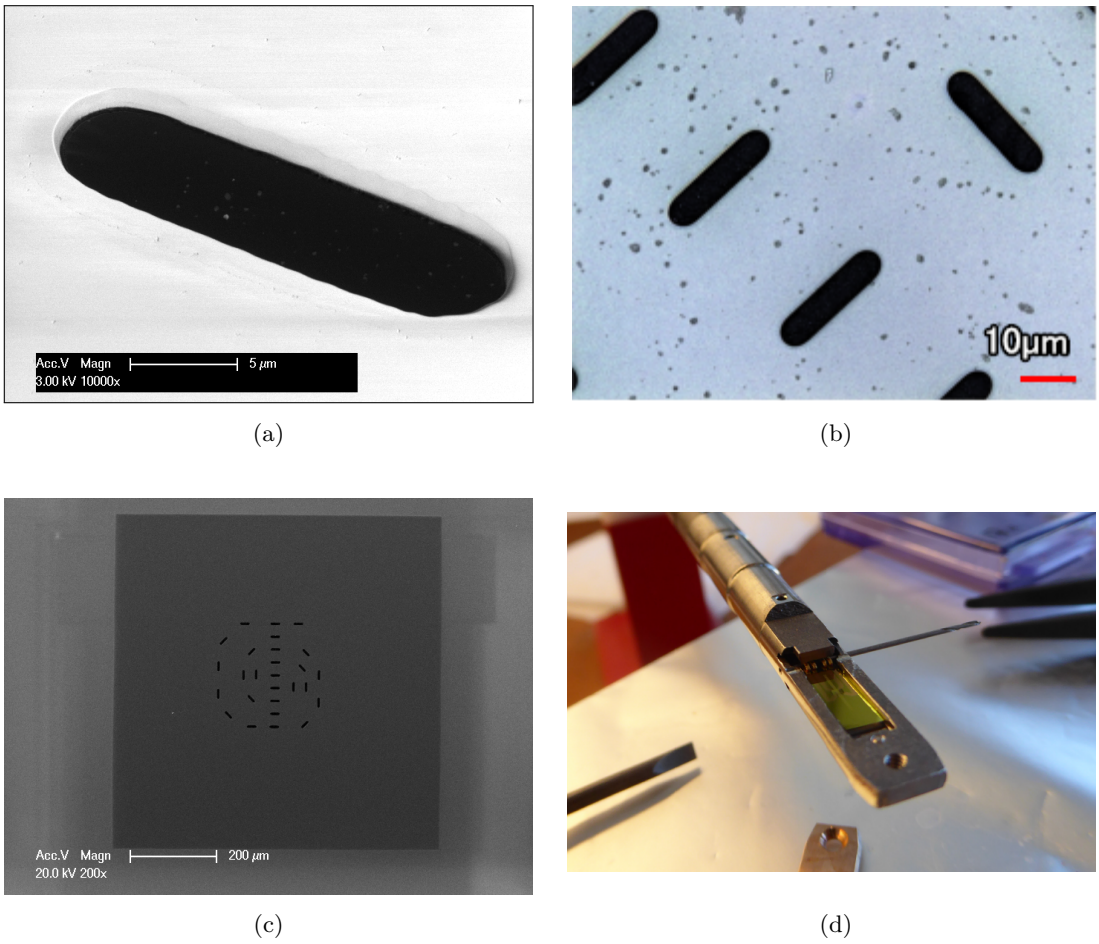

(a) (b)

(c) (d)

Figure 4.4: (a) tilted SEM image of an ETW, (b) an optical image 100x of a few ETWs with NPs sputtered on them, (c) a SEM image of the ETWs integrated in the supporting membrane and, (d) a die inserted in a TEM holder (abstracted from [1]).

4.4.1 Alumina

A silicon wafer coated with a 5 nm thick alumina film was measured before and after a 100 min VHF etch and no significant difference in thickness was measured. Remeasurement of wafers actually indicated a minute growth in the layer in the order of 0.1 nm. This may have been due to replacement error in the WOOLLAM.

4.4.2 TEOS

The step coverage of VHF was worse than anticipated. Figure 4.5 depict different variations of TEOS rings on top of the alumina windows. Figure 4.5a is an example of the non-uniform etch rate at dice-level. Windows less than 20 μm apart have different etch rates, as three of the windows have TEOS still completely intact on top of the alumina membrane. Figures 4.5b to 4.5d depicts various magnifications and angles of what are called TEOS rings in this thesis. The outermost ring that surrounds the window is typically always present. These rings follow the shape of the elongated circle perfectly, and as shown are never continuous, but corrugated and interrupted. The second, inner-ring is not always present. Sometimes it is continuous as seen below, or discontinuous. In figures 4.5c and 4.5d it is continuous and is lifted at their edges.

It is uncertain if actually TEOS that is seen, as additional etching, even at higher gas flows does not remove the rings. The reason for the TEOS ring's presence remains unknown. Reference [56] makes no mention of any remnants after TEOS etching in VHF. The solution to this issue was to limit the number of chips loaded in the VHF etcher at a given time.

This phenomenon was not present with the etching of the thermal SiO_2 from the back side. Besides material properties, there is a topological difference between the thermal silica and TEOS, as the alumina window is around 800 nm away from the surface of the SiN membrane – meaning the VHF has to enter a deeper cavity to etch the TEOS.

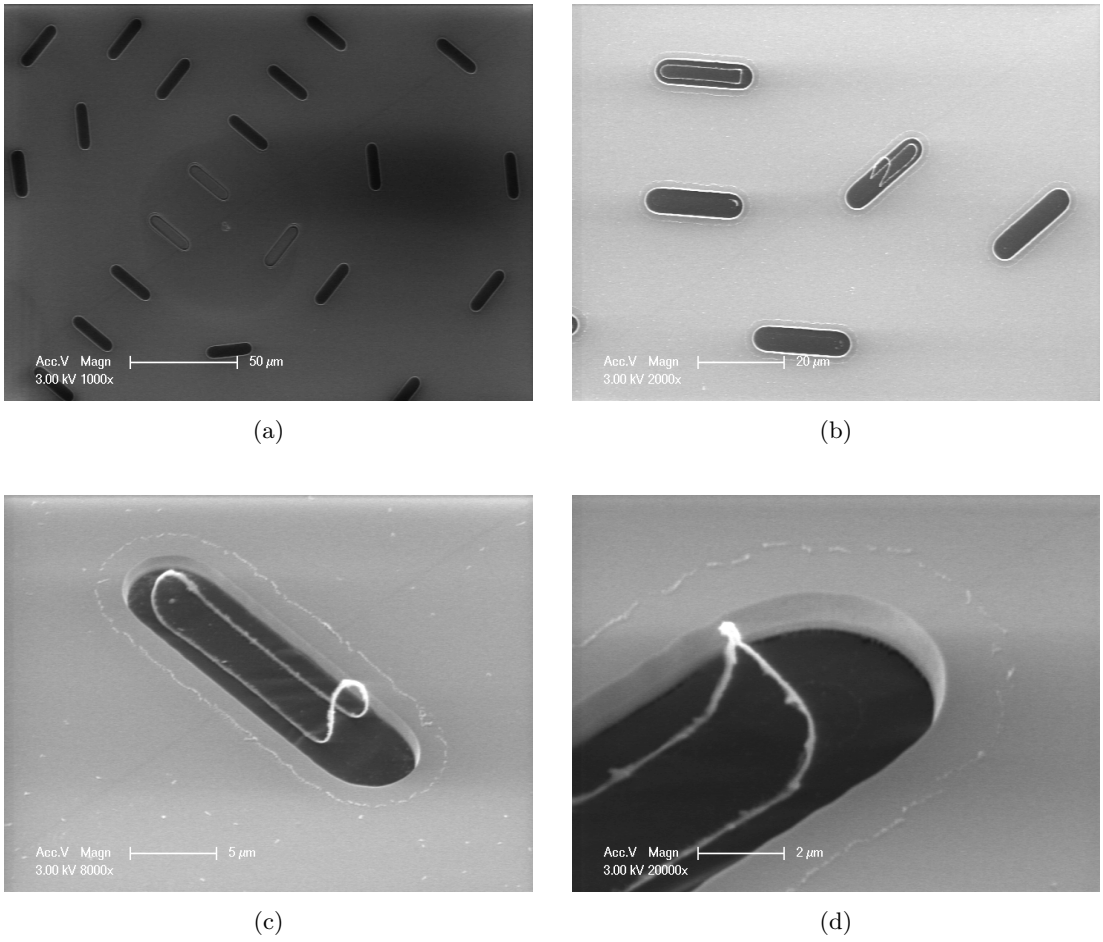

(a) (b)

(c) (d)

Figure 4.5: (a) an image showing released and un-released ETWs on the same dice, (b) an overview image of TEOS rings, (c-d) different angles and magnifications of TEOS rings at a tilt. All images were captured with a SEM.

In figure 4.6 an AFM image of a wafer with a 5 nm of ALD alumina, that had 1 μm of PECVD TEOS deposited and etched in VHF, is displayed. The full wafer was etched in the VHF system. The hillocks are dense and reach up to 30 nm in height. It is assumed that the hillocks seen in figure 4.6 are of similar origins from those in figure 4.5, which somehow relate to the TEOS deposition and etch. In [30], ALD alumina membranes of similar thickness were released, but with PECVD silica instead of TEOS. There is no mention of these hillocks in that work. Additionally, as mentioned earlier the rings in figure 4.5 only occur when more chips are loaded into the VHF at a time.

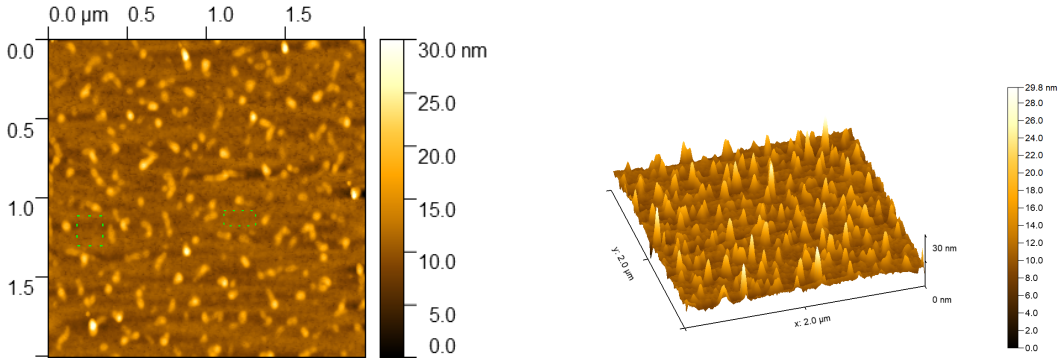

(a) (b)

Figure 4.6: (a) an AFM image of 5 nm alumina after TEOS deposition and removal in VHF, (b) a 3D reconstruction of (a).

The TEOS deposition and removal also thinned the alumina layer. While there are two oxides that are sacrificed in VHF, only TEOS was analyzed because it is deposited after ALD alumina. The alumina was grown on 200 nm of thermal silica at various thicknesses. A 1 μm thick layer of TEOS was subsequently grown on the alumina at 350°C. The TEOS was then etched in VHF for 10 cycles of 10 min each. The thickness of the alumina was measured before and after the TEOS deposition/removal. The results are given in table 4.1. To ensure that the VHF itself did not contribute to the thinning, the wafers were again etched by VHF and measured.

The removal of TEOS thinned the alumina layer by around 1 to 0.5 nm, depending on the thickness. The thinning of the alumina is likely caused by the temperature during the PECVD TEOS deposition. Thermal treatment of alumina will cause it to thin [31] and should be taken into consideration if the end-process ETW thicknesses are to be more accurately known.

Table 4.1: Thickness of alumina prior to TEOS deposition and after two separate VHF etching instances.

Avg Thickness Pre-TEOS Deposition (nm)	Avg Thickness after TEOS 10×10 min VHF (nm)	Thickness Difference (nm)	Avg Thickness after +10×10 min VHF (nm)	Thickness Difference (nm)
4.995	4.308	-0.687	4.405	+0.097
9.766	9.298	-0.468	9.298	0.000
15.154	14.187	-0.967	14.187	0.000
20.548	19.403	-1.145	-	-

4.4.3 Silicon Nitride

While the SiN support membrane is out of the scope of this thesis, it is still important to consider how the nanoreactor as a whole will be affected by the process done in this thesis. SiN deteriorates in VHF/EtOH by reacting with both the HF and EtOH to form ammonium fluorosilicate [$(NH_4)_2SiF_6$ / AFS]. Pyrolysis of AFS at 100°C or above will remove the compound over time [54].

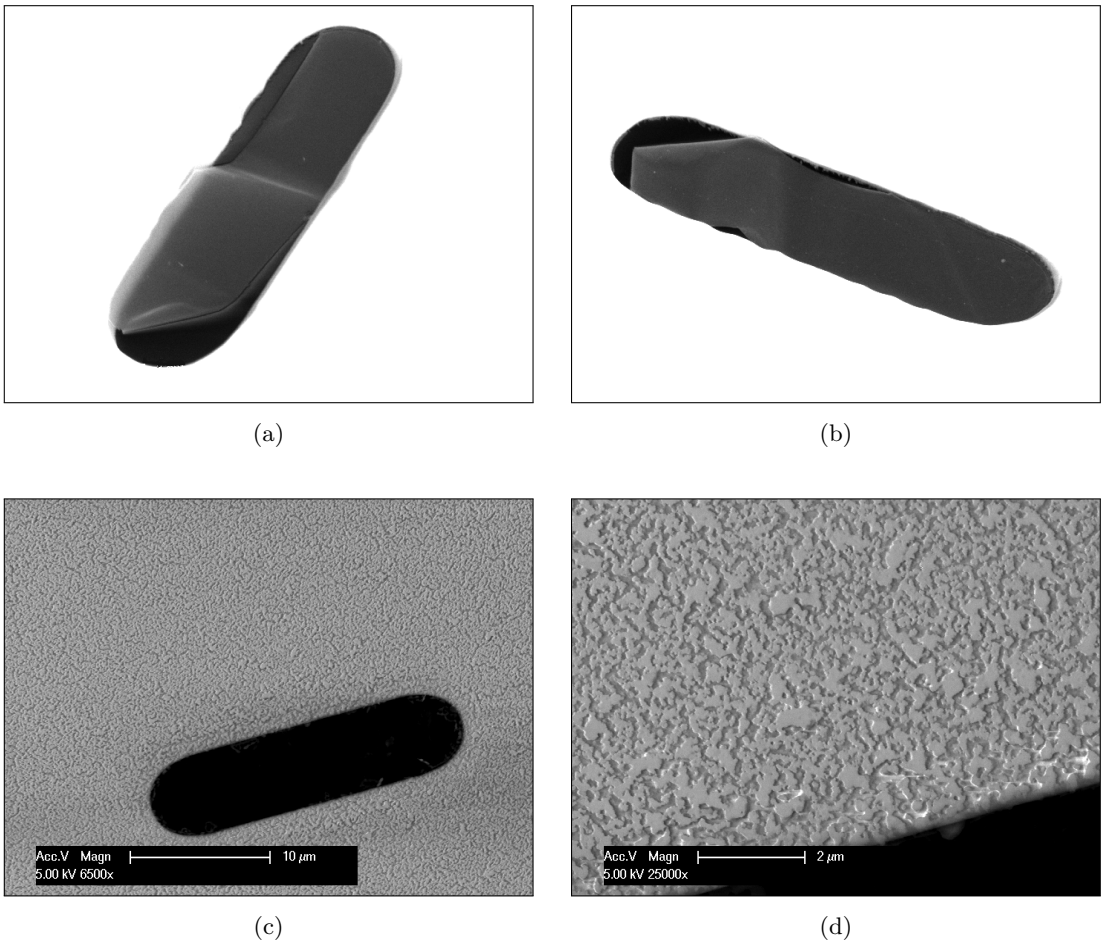

Figure 4.7: (a-b), SEM images (top-side) at 45° tilt showing the detachment of 5 nm ETWs from side walls. The contrast for these images is heightened in order to visibly distinguish the ETW and empty space. (c-d), SEM images from the backside of the device.

While AFS does not find itself directly on the ETWs and can be removed easily post-release, it should still be considered how this reaction can weaken the mechanical membrane. In some cases, the SiN membrane will break after VHF etching. The side-wall release of ETWs can be seen in figures 4.7a to 4.7b. In figures 4.7c to 4.7d the backside of the ETWs is displayed. Because there is no alumina protecting the SiN from VHF, material degradation is clearly visible.

4.4.4 Surface Uniformity

By cropping multiple areas like those boxed in the green-dotted line in figure 4.6a an average S_Q can be taken. This in attempt to take the RMS in the non-hillocked areas to determine how the TEOS deposition and removal affects the S_Q where hillocks do not form. The average S_Q was around 70 Å, which is slightly higher than the roughness ($S_Q = 40$) measured from figure 3.4 on pg. 19.

4.5 Residual Stress

The height profile of the 5 nm release ETWs can be seen in figure 4.8. The membrane is smoother than expected as none would expect a significant amount of bulging due to the compressiveness of Σ_{th}. Still, some bulging can be seen in the membrane.

Perhaps the geometry of the membrane can explain why the bulging may be suppressed.

Using the KEYENCE VK-X250 analyzer, the average height difference between the lowest and highest point in the three complete membranes captured in figure 4.7, was found to be 0.52 μm. The KEYENCE uses white-light informetry to measure the height differences.

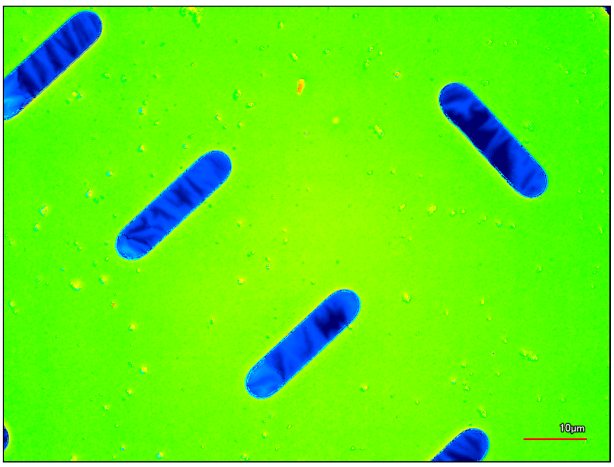

Figure 4.8: A height map of released 5 nm alumina ETWs.

4.6 Conclusions

The integration of ALD alumina within a nanoreactor process was successful, however there is always room for improvement. The SiN membrane mentioned in section 4.4.3 is undesired in VHF/EtOH. A solution to this problem would be replacing the SiN with SiC, which is a more chemically robust material [9]. SiC is completely resistant to VHF [57], which would fix the current degradation problem with SiN, and might also solve the TEOS ring problem shown in section 4.4.2.

Replacing TEOS with PECVD silica as the protective layer would also streamline the process. Silica is innate in TMAH, which means less mechanical handling and the ability to process in batches. This is because the whole wafer can be in contact with TMAH – without the use of single-sided holder. Silica also etches in VHF which means no changes are needed for the membrane release.

VHF has its limitations compared to wet etching. It is slow, and only a limited number wafers (4) can be loaded in the SPTS system at a time. No cassette-loadable VHF system seems to exist on the market. A more optimal process would use wet etching instead of VHF to release the membranes. Wet etching can etch oxides considerably quicker (e.g. BHF) and wafers can be etched in large (>25) batches. It is a requirement of the wet-etchant to have a high selectivity for alumina while also maintaining a low selectivity for silica. No standard clean room wet enchant [53] meets this requirement. The throughput of alumina integrated MEMS nanoreactors is limited not only by the ALD, but also the VHF system.

The next step would be to find another suitable ALD ETW material, more specifically one that is resistant to common wet etchants. ALD SiC (see [25] for precursor possibilities) is an ideal material because of its chemical inertness [9].

The last theorized improvement would be the integrating sacrificial and protective layers within the ALD system. A sacrificial layer can be grown encapsulating the ETWs during the same ALD run by using a different set of precursors before and after the ETW deposition. The ALD sacrificial layer should be resistant to TMAH or KOH and should also have an infinite selectivity (Sacrificial Layer : ETW) in an etchant to release the ETW.

5 MECHANICAL EXPERIMENTATION

5.1 Threshold Pressure

Pressure is an important requirement for nanoreactors during in-situ imaging, as it is a needed to increase the rate of catalytic reactions. The current industry standard for nanoreactors is 1 bar. The ETW geometry of this nanoreactor was not optimized for pressure because the shape is not a circle. Decreasing the surface area of the ETW will also naturally increase the pressure threshold, at cost of a smaller viewing area for the TEM user. While the geometries of ETWs vary, this test will provide a good reference to what can be expected from alumina at 5 and 15 nm thicknesses.

5.1.1 Methodology

The bulging test was performed on a modified experiment from [19]. An overview of this set-up is depicted in figure 5.1. The pressure is controlled and injected from an N_2 gas source. The gas is injected into a micro-machined metal holder which fits a distribution wafer. The distribution wafer forms a capillary system for the N_2 gas, which directs the gas to 40 designated areas which correspond to 40 TMAH windows on a nanoreactor test wafer. The idea behind this contraption is to control the pressure of gas from the source and distribute it equally among all 40 membranes.

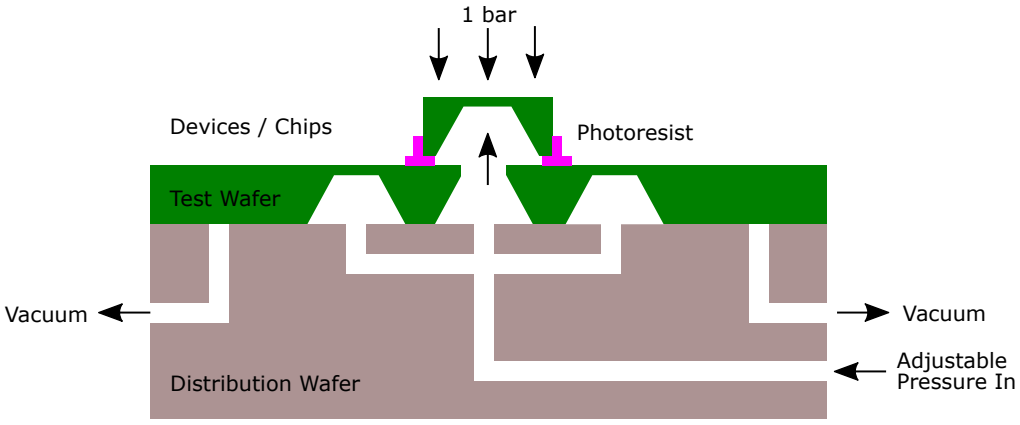

Figure 5.1: A cross-sectional view of the set-up for the pressure threshold experiment. The metal holder is not depicted in this illustration.

Working from this, 4 membranes were purposely broken on a test wafer. On top of these broken holes, the nanoreactor devices tested in this experiment are aligned then glued into place by placing and baking photoresist. The chips are gently nudged by a tweezer to ensure that the chips are glued in place. A vacuum ensures that the test wafer is fixed to the distribution wafer.

The KEYENCE's differential interference contrast (DIC) and white light interferometry was used to verify if windows are broken are not. The pressure was increased in increments of 0.25 bars. Bulging of the support membrane confirmed that the ETWs were indeed subjected to pressure. This set-up is limited to 1.25 bars.

5.1.2 Results and Conclusion

The 5 and 15 nm alumina windows survived up to 0.75 bars and 1.25 bars respectively. The 15 nm may exceed 1.25 bar, however due to set-up limitations, it could not be tested. The 5 nm windows can withstand less pressure than 1 bar, performing worse than current standards.

In figure 5.2 a 3D reconstruction of a height map and a DIC image is shown. The bulging in some cases is predominant on one side of the ETW only. The windows are dirty, which allowed to ETWs to be detected easier in an optical microscope. Notice in the DIC image in figure 5.2 that there is a roughness on the windows. Figure 5.3 shows a pair of images taken from a chip with ETWs that are in some cases broken. In contrast to figure 5.2b, figure 5.3b has a perfectly smooth surface in some ETWs, indicating that they are broken, as there is now no reflection in those areas.

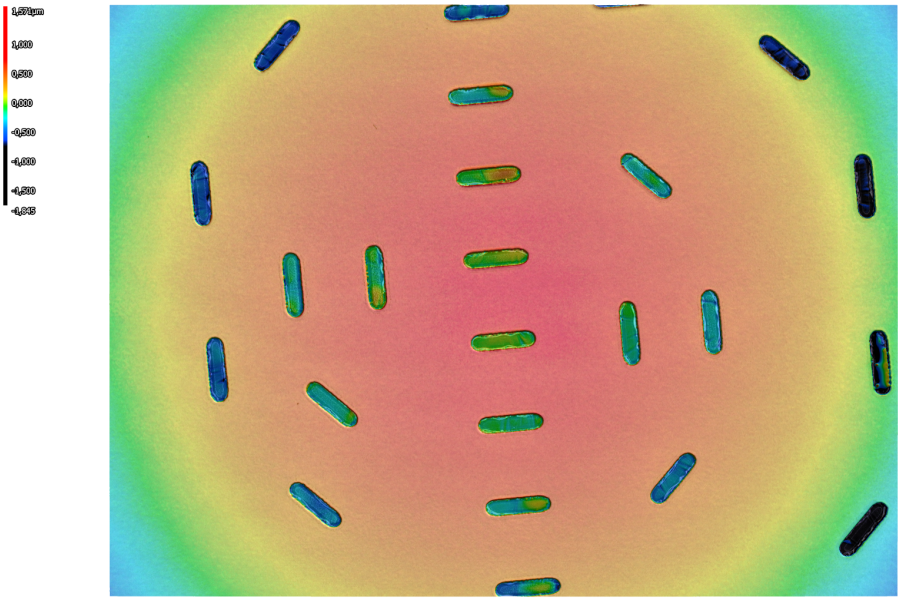

(a)

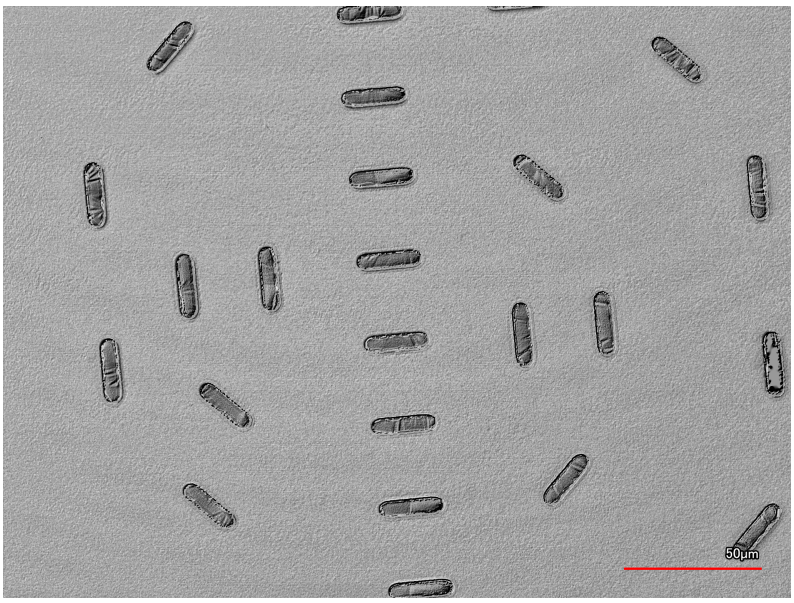

(b)

Figure 5.2: (a) a height map and, (b) DIC image of unbroken 15 nm ALD alumina ETWs.

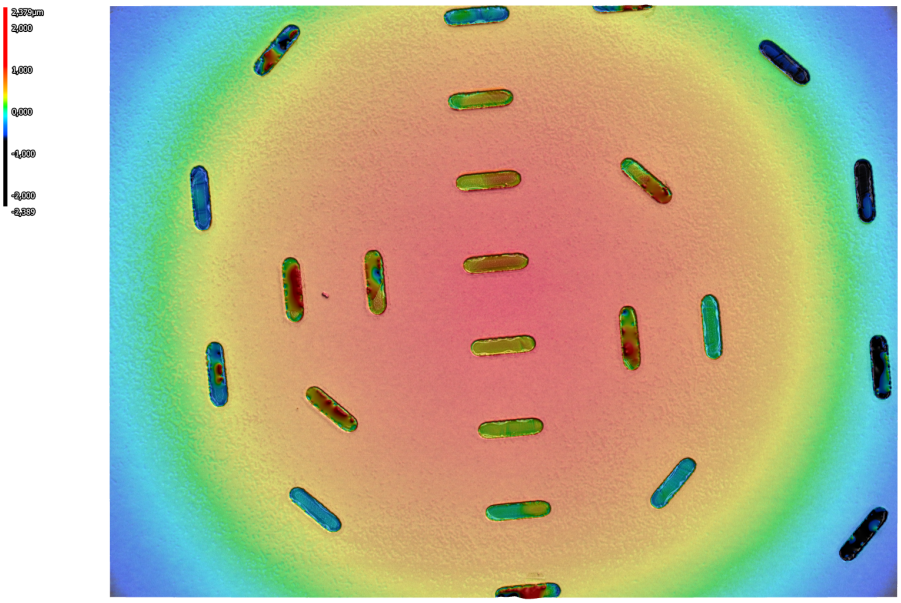

(a)

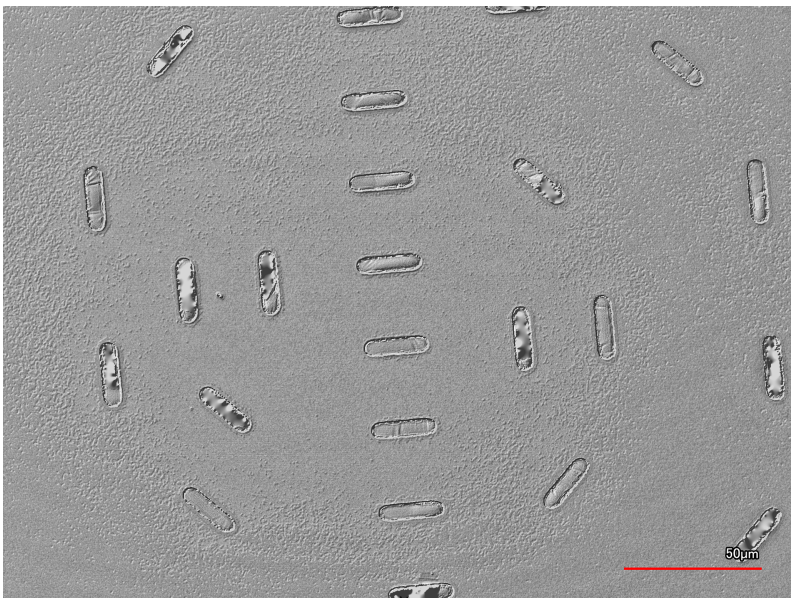

(b)

Figure 5.3: (a) a height map and, (b) DIC image of unbroken and broken 15 nm ALD alumina ETWs. A few ETWs have high height variances in (a), or appear very smooth in (b), indicating that they are broken.

6

ELECTRON IMAGING EXPERIMENTATION

In this chapter, two different deposition methods are explained in section 6.1. Next, transparency comparisons between alumina and SiN ETWs are made and discussed in section 6.2. Lastly, conclusions are given in section 6.3.

6.1 Sample Preparation

Two different NPs were imaged in a TEM, each of them deposited differently.

– Liquid Suspension

This is currently the most commonly used method to deposited NPs on ETWs. NPs are mixed into a liquid solution, dropped onto the nanoreactor, and left to evaporate. In this thesis, 2 drops from a copper NP solution was mixed with 5 mL of H_20, and 20 mL of ethanol in a beaker. This beaker was then placed in an ultrasound tank for one hour and covered, to limit the evaporation of the liquid. This step dispersed the particles, as these particles have a tendency to coagulate in still solutions.

One drop of this solution is then placed on the backside of the supporting membrane and left to evaporate. TEM images of copper NPs can be seen in figure D.2.

– Spark Ablation

Spark ablation creates NPs by generating high voltages (1.5 kV) between metal electrodes. Once the voltage potential is high enough, a spark is generated between the electrodes. This spark will discharge NPs, which can be sputtered with a carrier gas directly onto the nanoreactor [58].

A benefit of this technology is that the electrode material can be almost any conductive material. In this case nickel (Ni) was used. Like any metal, Ni will slightly oxidize with contact to air, meaning that the nickel deposited will also contain a nickel oxide (NiO) phase. Another benefit is more control of the deposited NPs, since the density and size of the NPs are related to carrier gas selection, gas-flow and electrode voltage [58]. Additionally, since they can be guided with N_2, there is minimal risk of contamination. It was initially uncertain if NPs could be deposited via this method onto the ETWs, since the pressure of the carrier gas was unknown. The 5 nm ETWs were able to survive the deposition, which was confirmed in a SEM.

6.2 Electron Transparency

6.2.1 Theoretical Expectations

From theory in chapter 2 and data from table 2.1 on page 14, the relative scattering factor K of 10 nm ALD alumina is 73% lower than that of 15 nm SiN. In TEM images, the more strongly the ETW scatters electrons, the darker the image will become as

fewer electrons will reach the objective lens. In the case of the SEM, ETWs that are less electron-transparent will become brighter, since only reflected electrons are detected.

6.2.2 TEM

The samples were tested in a FEI Tecnai at 200 keV. Ideally, the resolution would be quantitatively measured by observing the FFT of crystalline NPs on the ETWs. However, with the availability of only amorphous NPs the intensity differences between ETWs under identical TEM conditions were compared. The 5 nm alumina windows disintegrated immediately under the electron beam. This indicates that 5 nm thick membranes are unsuitable as a nanoreactor ETWs. It was incorrectly hypothesized that thinner ETWs would be more resistant to electron beams as $\sigma_{inelastic}$ decreases exponentially with lower thicknesses. Alumina membranes 10 nm thick did survive the TEM session, which was imaged and inspected for around 20 min. During the imaging session no charging on the ETWs was noticed.

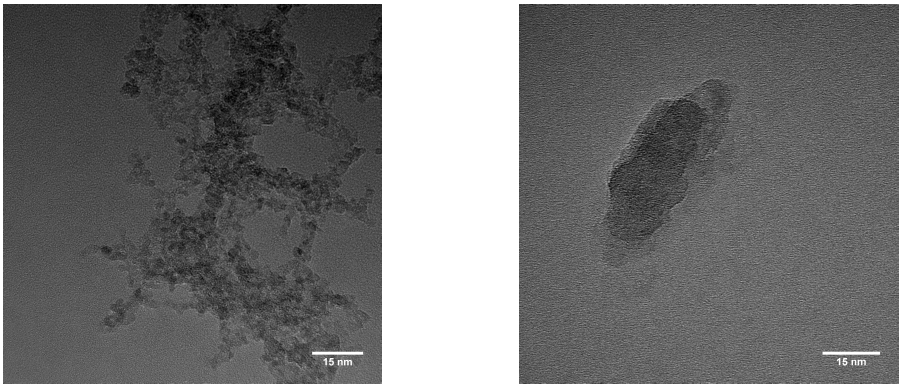

(a) (b)

Figure 6.1: (a) A NP imaged on a 15 nm SiN ETW, (b) a NP imaged on a 10 nm alumina ETW. Both images are taken in identical conditions at 450kx magnification.

To measure the differences in electron transmission between 15 nm SiN and 10 nm alumina, GWIDDION was used to find the mean value for contrast (16-bit, signed grey-scale value) in the clear regions in figure 6.1a and figure 6.1b, which is a 15 nm SiN and 10 nm alumina ETW respectively. In the images no objective aperture was used, thus contrast behavior was not implicitly controlled. The average contrast value for the 10 nm alumina and 15 nm SiN ETWs were 737 and 233 respectively.

6.2.3 SEM

While the application of ETWs in this thesis is intended for TEM imaging, by using a SEM the transparency is more noticeable. Unlike the TEM, the SEM uses backscattered electrons $\alpha > \pi/2$ of in-elastically scattered electrons (ISE) to form images. SEMs raster scan a specified area while using a +200V biased cathode to absorb charge at a given pixel. The amount of charge is related to the amount of ISEs generated. Because each pixel is generated one at a time the SEM automatically adjusts the contrast relative to what has already been raster-scanned. ISEs are able to be detected in this method because of the significant energy loss after collision [59].

Electrons are also elastically back-scattered to the chamber wall. These back-scattered electrons (BSEs) have a probability of generating ISE after collision with the chamber wall (figure 6.2) [59]. Typically a back scattering detector (BSD) can be placed inside

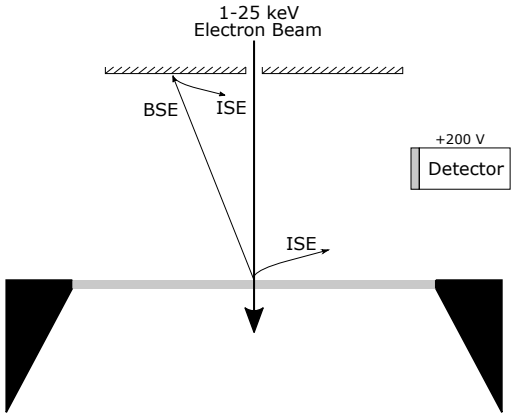

Figure 6.2: BSE and ISE scattering and detection in a SEM.

a SEM to detect only the BSEs. This was not available in the EKL. In any case, by comparing the contrast of different membranes, the difference in transparency can be clearly demonstrated. The film must be free-standing with a large, open space beneath it. All electrons transmitted through the membrane should be absorbed so it does not contribute to the cathode charge. Additionally, The window should also be imaged entirely. This is to minimize the auto-adjustments the SEM makes. Because the SiN and alumina samples had different supporting membrane thicknesses, comparing the contrast between the supporting membrane and ETW would not be possible. The contrast and brightness adjustments were kept constant for all images.

(a) (b)

Figure 6.3: (a) a 5 nm alumina and (b) a 15 nm SiN ETW imaged in a SEM at 50,000 kx magnification and 15 keV. (a) has a grey-scale average of 23.1, while (b) has a grey-scale average of 47.2 (8 bit, unsigned).

(a) (b)

Figure 6.4: (a) a 5 nm alumina and (b) a 15 nm SiN ETW imaged in a SEM at 50,000 kx magnification now at 5 keV. (a) has a grey-scale average of 13.2, while (b) has a grey-scale average of 42.7 (8 bit, unsigned).

Figure 6.3 and Figure 6.4 are comparisons between the 5 nm alumina and 15 nm SiN ETWs at 15 and 5 keV respectively. Since the SEM uses back-scattering to form images, the darker the image the more electron-transparent it is. The 5 nm alumina ETWs are clearly darker than their counterparts.

6.3 Conclusions

The transparency of thinner ALD alumina membranes was qualitatively compared to 15 nm SiN membranes in a TEM and SEM. In both cases, as predicted from theoretical calculations, the thinner ETWs proved to be more electron-transparent.

7

CONCLUSIONS AND FUTURE WORK

In this thesis the process for releasing 5 nm ALD alumina suspended membranes – specifically for nanoreactor applications – was described and carried out. ALD membranes exhibit desirable qualities for TEM imaging applications due to their uniformity, continuity and thickens control at ultra-thin thicknesses.

There are a couple ways that the process can be improved. SiC should replace SiN for the supporting membrane, as SiN is slowly degraded in VHF. Replacing PECVD TEOS with PECVD silica is a logical improvement. This change allows for bulk etching in TMAH, as a single-sided holder would no longer be needed. VHF is considered a weakness in this process, as wet etching the clear winner for consistent, bulk processing. However, there is no reason that a bulk VHF etchant system can be designed and routinely used. Because alumina and SiC are completely resistant to VHF, the batch can be over-etched to ensure all membranes are released. Lastly, ALD can preform the depositions of the ETW and sacrificial layers during the same deposition run, encapsulating the ETW.

There is a limit to how thin ETWs can be. Alumina ETWs that are 5 nm thin disintegrate immediately under the beam's flux, even low intensities. A flux vs. survival time experiment was not explicitly carried out. However, the 10 nm alumina ETWs were able to be imaged in a 20 min session without any degradation. It is unpredictable where between a thickness of 5 to 10 nm an optimization lies between survival time and electron-transparency.

Spark ablation is a proven and better method for depositing NPs on ETWs. Ultra-thin ETWs can survive this deposition method. Spark Ablation allows for a TEM user to have direct control on material and deposition density. Additionally, the NP can be carried in N_2.

The threshold pressure pressure of 15 nm alumina is only slightly better (1.25 bar) than current ETWs. The ETWs can certainly hold more pressure if they were circular and have a smaller surface area.

While in this thesis alumina was used as ETW materials, any ALD material would be suitable if can be controlled with etchants. This means that there are many options in material selection to the whim of the process engineer. While the application of ultra-thin membranes in this thesis is intended for nanoreactors, there are many other areas where this process can be applied – such as sensors or tynodes.

A

ADDITIONAL ELECTRON IMAGING TOPICS

A.1 Modifications to Rutherford's Cross Section

There are two problems with the formula in equation (2.14a). First, is that as $\theta \to 0$ the DSC diverges to infinity. This will be fixed by adding the screening effect. Electron screening is when the atom appears slightly less positive to the electron due to the electron cloud surrounding it. A screening modifier $\frac{\theta_0^2}{4}$ is added. θ_0 is known as the screening parameter:

$$\theta_0 = \frac{0.117Z^{1/3}}{E_0^{1/2}} \tag{A.1}$$

The screening effect is added to the angular component so that now:

$$\frac{d\sigma}{d\Omega_R} \propto \frac{1}{(sin^2\frac{\theta}{2} + \frac{\theta_0^2}{4})^2} \tag{A.2}$$

Screening (electron-electron interaction) is then mostly dominant in low scattering angles, while above θ_0 electron-nucleus interaction become dominant.

The second modification is moving from non-relativistic to relativistic effects because of the high energies supplied. Because of the higher energy, the electrons become heavier and faster relative to the speed of light. Using the relativistic equations becomes more important as the energy of the electron approaches the rest energy m_0c^2. The relativistic equation for energy is the sum of the electrons rest energy and kinetic energy (qE_0) supplied by the TEM:

$$E = mc^2 = qE_0 + m_0c^2 \tag{A.3}$$

m_0 is the rest mass of an electron, m is the relative mass of the electron, c is the speed of light, Γ is the Lorentz factor (1+qE$_0$/E):

$$m = m_0\ 1 + \frac{E}{E_0} \tag{A.4a}$$

$$v = c\sqrt{1 - \frac{1}{\Gamma^2}} \tag{A.4b}$$

$$\lambda_r = \frac{h}{m_0 \cdot c}\frac{\Gamma}{\sqrt{1-\Gamma^2}} \tag{A.4c}$$

The relativistic CS, in it s various forms:

$$\frac{d\sigma}{d\Omega_R} \propto \left(k_0\frac{Z \cdot q^2}{8\pi \cdot mv^2}\right)^2 \equiv \left(\frac{Z \cdot \Gamma \cdot \lambda^2}{8\pi^2 \cdot a_0}\right)^2 \tag{A.5}$$

Where a_0 is the Bohr radius (= 0.029 nm)

In literature, there are multiple derivations and modifications for Rutherford's CS. The derivations above completely ignore the wave-like nature of electrons, which introduce inaccuracies.Rutherford's formula is special because the same result can be from classical mechanics as well as quantum mechanics.

A.2 Scattering Contrast

Contrast is the difference in intensity n, of two areas in an image. Transmission (electron flux) is controlled by σ_R equation (2.14a) of a material and the acceptance angle α equation (2.4). Electrons are scattered outside the objective aperture ($\theta > \alpha$) are absorbed by it. Only electrons with deflection angle $\theta < \alpha$ are transmitted. This is called bright-field mode. In a SEM, contrast can be change willfully before taking an image by, for example, changing detector gain. Even though TEMs use CCD cameras they are strictly analog machines. To simplify calculations, the aperture of the incident beam α_i is much smaller than α, so that $\alpha_i << \alpha$. When trying to image NPs on a similarly thick film more contrast is always better as the NPs can be better distinguished from the film.

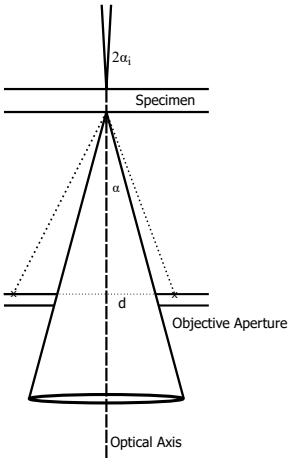

Figure A.1: An electron beam approaching a specimen at angle α_i is scattered by the specimen. Electrons scattered more than α do not contribute to the transmission of the image. The objective lens between the specimen and the object aperture is not included in this illustration.

The transmission from two areas will now be calculated: the electron path passing the NP and film, and the path passing the film only. The film and NP will have a MPF of Λ_f and Λ_n respectively.

$$n_{n,f} = n_0 exp(-(\frac{z_t}{\Lambda_t} + \frac{z_n}{\Lambda_n})) = n_0 exp(-\frac{z_t}{\Lambda_t}) \cdot n_0 exp(-\frac{z_n}{\Lambda_n}) \tag{A.6a}$$

$$n_f = n_0 exp(-\frac{z_t}{\Lambda_t}) \tag{A.6b}$$

Contrast can be quantitatively determined in different metrics:

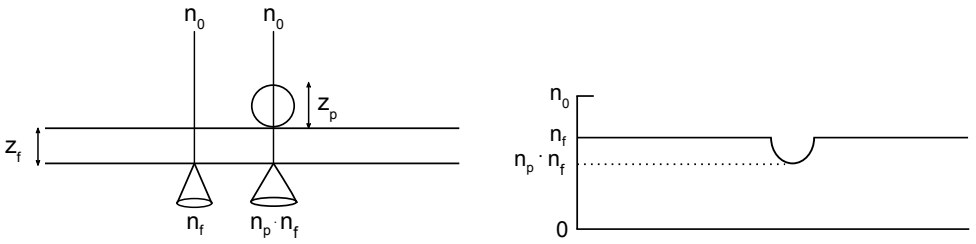

(a) (b)

Figure A.2: (a) An unscattered electron beam n_0 passing though both a thin film and thin film + NP results in transmittances n_f and $n_{p,f}$. (b) A comparison between transmittance of n_0, n_f and $n_{p,f}$.

$$C_M = \frac{n_{f,n} - n_f}{n_{f,n} + n_n} \qquad \text{Michelson contrast, used in [14].} \tag{A.7a}$$

$$C_W = \frac{n_{f,n} - n_f}{n_{f,n}} \qquad \text{Weber contrast, used in [11].} \tag{A.7b}$$

$$C_0 = \frac{n_f}{n_{f,n}} \qquad \text{Normal contrast, used in [17].} \tag{A.7c}$$

Solving for equation (A.7) with equations (A.6a) and (A.6b) results in all of the contrasts being dependent on n_p only. It is then impossible to compare the effectiveness of ETWs using contrast.

(a) (b) (c)

Figure A.3: Three images, all with identical contrast ratios. The circular symbols have identical transmittances in each image. Each background has a different transmittance. While all three are identical w.r.t contrast, it is obvious that (x) is the clearest.

B

LIST OF ABBREVIATIONS, SYMBOLS, AND UNITS

-OH	hydroxl group
AFM	atomic force microscope/y
AFS	ammonium fluorosilicate
ALD	atomic layer deposition
Al_2O_3	aluminum oxide / alumina
BHF	buffered HF
CCD	charge coupled device
CO	carbon monoxide
CS	cross section
CTE	coefficient of thermal expansion
DCS	differential cross section
DIC	differential interference contrast
DP	diffraction pattern
EDX	energy-dispersive X-ray spectroscope/y
EKL	Else Kooi Laboratory
ETW	electron transparent window
EtOH	ethanol
FFT	fast fourier transform
GPC	growth per cycle
HF	hydrogen fluoride
HRTEM	high resolution TEM
LPCVD	low pressure chemical vapor deposition
LPF	low pass filter
MEMS	micro electrical-mechanical system/s
MPF	mean free path
NA	numerical aperture
NP	nano-particles
PDF	probability distribution function

PECVD	plasma enhanced chemical vapor deposition
RI	refractive index
RMS	root mean squared
RSD	relative standard deviation
SEM	scanning electron microscope/y
SiC	silicon carbide
SiN	silicon nitride
SiO_2	silicon dioxide / silica
TCS	total cross section
TEM	transmission electron microscope/y
TEOS	tetraethyl orthosilicate
TMA	trimethyl-aluminum
TMAH	tetramethylammonium hydroxide
VHF	vapor HF
VLM	visual light microscope/y

Symbol	Name	Units
$\frac{d\sigma}{d\Omega}$	differential cross section	meter^2
α	acceptance angle	degree / radian
σ	cross section	meter^2
λ	wavelength	meter
Λ	mean free path	meter^{-1}
δ	resolving power	meter
ρ	material density	kilogram·meter^{-3}
ν	Poisson's ratio	
γ	free surface energy	joule·meter^{-2}
Γ	Lorentz factor	
η	coefficient of thermal expansion	Celsius^{-1}
Σ	mechanical stress	pascal
α_i	incident angle	degree / radian
σ_t	total cross section	meter^2
A	standard atomic weight	u
B	magnetic field	tesla
E	Young's Modulus	pascal
E_0	electron kinetic energy	q·volts
E_i	electron kinetic energy	volt·$meter^{-1}$
K	atomic scattering factor	
V	acceleration voltage	volts
Z	atomic number	
d	objective aperture diameter	meter
f	focal point	meter
h	thickness (general)	meter
v	relative electron velocity	meters·second^2
3D	3-dimensional	

Millimeter (mm)	$\times 10^{-3}$ meter
Micrometer / Micron (μm)	$\times 10^{-6}$ meter
Nanometer (nm)	$\times 10^{-9}$ meter
Angstrom (Å)	$\times 10^{-10}$ meter
Picometer (pm)	$\times 10^{-12}$ meter
ϵ_0, vacuum permittivity	8.854×10^{-12} farad·meter^{-1}
c, speed of light	2.9979×10^{8} meters·second^{-1}
m_0, rest mass	9.1091×10^{-31} kilogram
q, elementary charge	1.602×10^{-19} coulomb
h, Plank's constant	6.6256×10^{-34} joule·second
k_0, Coulomb's constant	8.988×10^{9} newton·meter^2
N_A, Avogadro' constant	$6.022140857 \times 10^{23}$ mol^{-1}
b_0, Bohr's Radius	0.029 nm

C

PROCESS SPECIFIC ETCH RATES

Material	Etchant	Etch Rate	Time Etched
TEOS / Thermal SiO_2	Al Etch[a] at 35°C	0	4 min
TEOS	Vapor HF[bc]	55.95 nm/min	5 min
Thermal SiO_2	Vapor HF[bc]	12.25 nm/min	5 min
ALD Alumina	Vapor HF[bc]	0	100 min
ALD Alumina	Al Etch[a] at 35°C	1.08 nm/min	4 min
ALD Alumina	BHF 7:1[d]	1.35 nm/sec	11 sec
ALD Alumina	HF 0.55%[d]	0.29 nm/sec	30 sec
ALD Alumina	Phosphoric Acid at 157°C	1.08 nm/sec	12 sec

a 77% H_3PO_4+11%HNO_3+3%HAc
b Temperature is unknown, holder feels warm after an etching run
c Vapor HF with EtOH as catalyst, etched for 5nm. flow rates: EtOH/210 sccm; HF/190 sccm, pressure: 125 Torr
d Room Temperature

D

SUPPLEMENTARY IMAGES

D.1 Film Verification - SEM

If the film is so thin, how can we verify that the film is actually there? Two main methods were used to determine if a window actually existed or not. Due to the nanoscale thickness, it's impossible to verify if windows exist using an optical microscope at 100x magnification. Dirty of contaminated windows can be seen optically due to the reflection of the micro-sized particles. Because of the high bulging due to the stress, it is able to verify the existence 15 nm windows buy finely adjusting the focus up and down the window to see bulging and folding of the membrane. For 5 nm the clearest way was to use a SEM. In figures D.4a and D.4b, an 20 keV and 0.5 keV SEM image respectively, of 5 nm alumina ETWs were taken at similar locations on the same chip. There are two broken windows in the top left corner. In figure D.4a its hard to tell if a thin film exists there or not, however at lower energies (figure D.4b) the back-scattering coefficient increases considerably such that the contrast between broken and unbroken windows becomes obvious (equation (2.14)). The elastic back-scattering coefficient can be calculated using equation (2.7) and taking the limit of integration from $\pi/2$ to π.

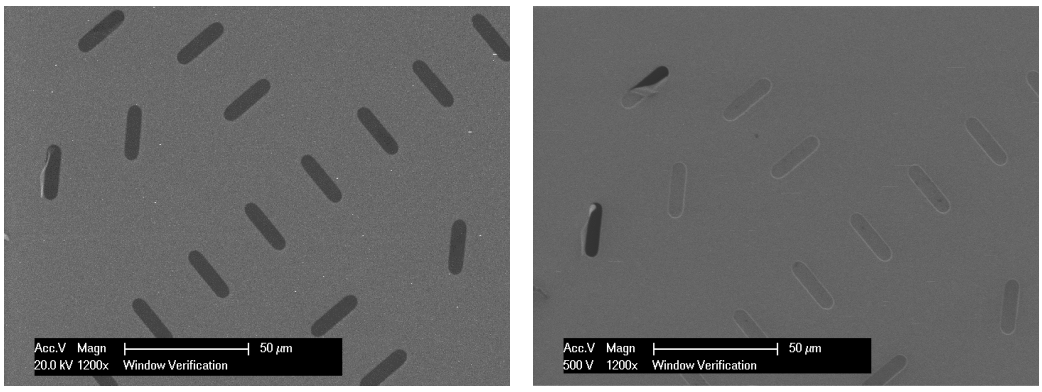

(a) (b)

Figure D.1: Two SEM images taken at a similar area on the same chip, taken at different energies.

D.2 Film Verification - TEM

To prove that 10 nm ALD alumina windows were imaged in the TEM, an EDX spectrograph was made. The graph can be seen in figure D.3.

D.3 Attempt in releasing sub-1 nm thick ALD membranes

What happens if we grow 10 cycles of ALD alumina and try to release it? The results are depicted in figure D.4. The alumina seems to curve up into itself. The layer did not fully coalesce, which is visible by the number of pin-holes in the layer. Magnifying further onto the alumina will cause the film to deform and bend. Not depicted is the surface of the SiN membrane. It looks similar to the AFS contaminated layer captured in figure 4.7d.

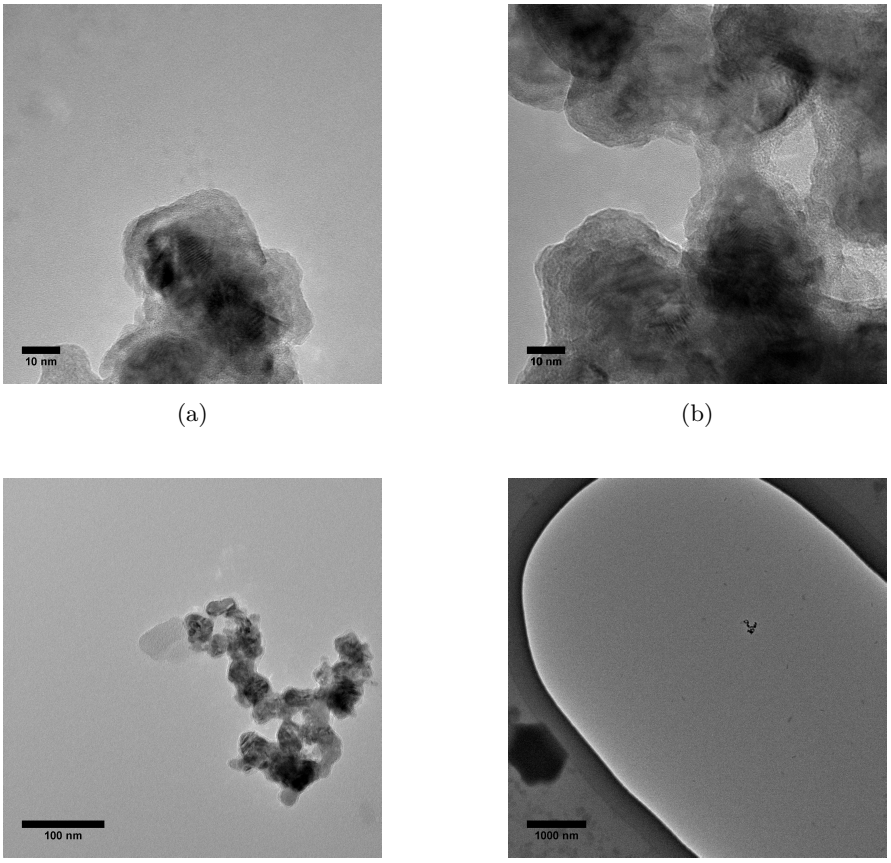

(a) (b)

(c) (d)

Figure D.2: The same copper NP imaged at different magnifications in a TEM.

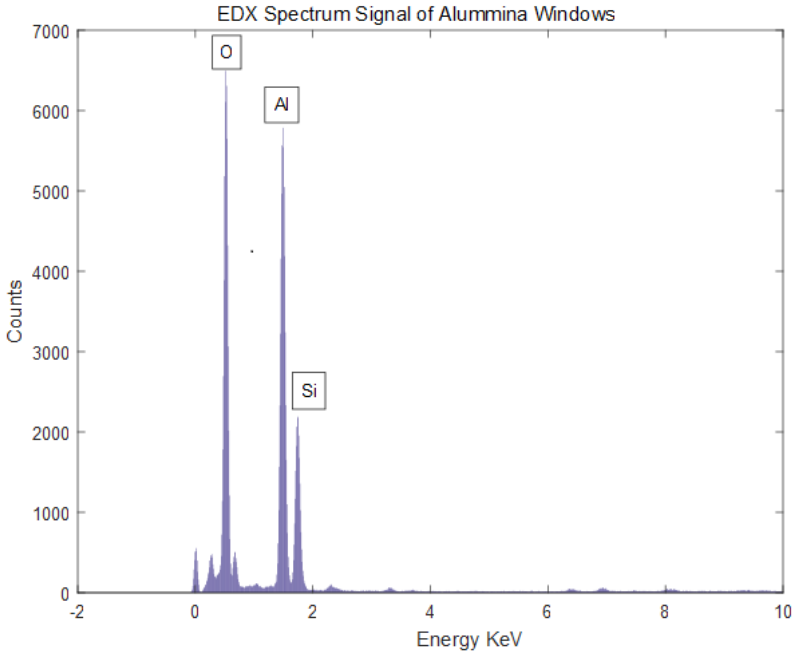

Figure D.3: EDX spectograph of a 10 nm alumina window

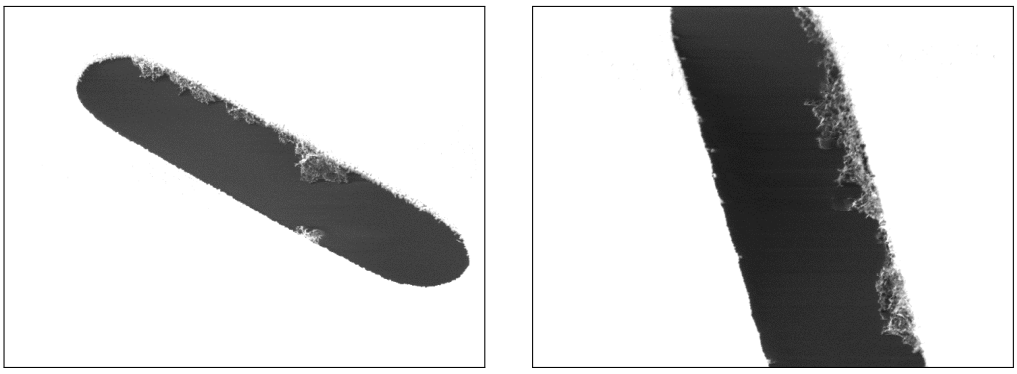

(a) (b)

Figure D.4: Ten cycles of ALD alumina deposited and released in VHF.

BIBLIOGRAPHY

[1] Bremmer Gerrit Mainus. "Transmission Electron Microscopy on live catalysts." PhD thesis. University of Leiden, 2017.

[2] Fan Yang et al. "Understanding nano effects in catalysis." In: National Science Review 2.2 (2015), pp. 183–201. doi: 10.1093/nsr/nwv024. eprint: /oup/backfile/content_public/journal/nsr/2/2/10.1093_nsr_nwv024/3/nwv024.pdf. url: +http://dx.doi.org/10.1093/nsr/nwv024.

[3] Xiaowei Xie et al. In: Nature 458.7239 (2009), 746–749. doi: 10.1038/nature07877. url: https://www.nature.com/articles/nature07877.

[4] Shuai Tan and Dongmei Li. "Enhancing Oxygen Storage Capability and Catalytic Actifvity of Lanthanum Oxysulfide (La2O2S) Nanocatalysts by Sodium and Iron/-Sodium Doping." In: ChemCatChem 10.3 (2018), pp. 550–558. issn: 1867-3899. doi: 10.1002/cctc.201701117. url: http://dx.doi.org/10.1002/cctc.201701117.

[5] L. Mele et al. "A molybdenum MEMS microhotplate for high-temperature operation." In: Sensors and Actuators A: Physical 188 (2012). Selected papers from The 16th International Conference on Solid-State Sensors, Actuators and Microsystems, pp. 173 –180. issn: 0924-4247. doi: https://doi.org/10.1016/j.sna.2011.11.023. url: http://www.sciencedirect.com/science/article/pii/S0924424711006820.

[6] Vinod Kumar Khanna Mahanth Prasad Dhairya Singh Arya. "Fabrication and reliability study of a double spiral platinum-based MEMS hotplate." In: Journal of Micro/Nanolithography, MEMS, and MOEMS 14 (2015), pp. 14 –14 –9. doi: 10.1117/1.JMM.14.2.025003. url: https://doi.org/10.1117/1.JMM.14.2.025003.

[7] J. Fredrik Creemer et al. "A MEMS Reactor for Atomic-Scale Microscopy of Nanomaterials Under Industrially Relevant Conditions." In: Journal of Microelectromechanical Systems 19.2 (2010), 254–264. doi: 10.1109/jmems.2010.2041190.

[8] Héctor Hugo Pérez-Garza et al. "The "Climate" system: Nano-Reactor for in-situ analysis of solid-gas interactions inside the TEM." In: Nano/Micro Engineered and Molecular Systems (NEMS), 2016 IEEE 11th Annual International Conference on. IEEE. 2016, pp. 85–90.

[9] Bruno Morana. "Silicon Carbide Thin Films for MEMS Nanoreactors for in-situ Transmission Electron Microscopy." PhD thesis. Technical University of Delft, 2015.

[10] Solutions for In Situ Electron Microscopy. url: http://denssolutions.com/.

[11] David B. Williams and C. Barry. Carter. Transmission electron microscopy: a textbook for materials science. Springer, 2008.

[12] R F Egerton. Physical Principles of Electron Microscopy An Introduction to TEM, SEM, and AEM. Springer Verlag, 2016.

[13] Francis Graham. Smith and John Hunter. Thomson. Optics. Wiley, 1996.

[14] Jurgen Thomas. Analytical Transmission Electron Microscopy, An Introduction for Operators. Springer, 2016.

[15] Wei-Kan Chu, James W. Mayer, and Marc-A Nicolet. Backscattering spectrometry. Academic Press, 1978.

[16] Professor E. Rutherford F.R.S. “LXXIX. The scattering of and particles by matter and the structure of the atom.” In: The London, Edinburgh, and Dublin Philosophical Magazine and Journal of Science 21.125 (1911), pp. 669–688. doi: 10.1080/14786440508637080. eprint: https://doi.org/10.1080/14786440508637080. url: https://doi.org/10.1080/14786440508637080.

[17] L. Reimer and H. Kohl. Transmission electron microscopy: physics of image formation and microanalysis. Springer, 2008.

[18] M. P. Mintchev F. M. Bui K. Bott. “A quantitative study of the pixel-shifting, blurring and nonlinear distortions in MRI images caused by the presence of metal implants.” In: Journal of Medical Engineering & Technology 24.1 (2000), pp. 20–27. doi: 10.1080/030919000294003. eprint: https://doi.org/10.1080/030919000294003. url: https://doi.org/10.1080/030919000294003.

[19] Sarat Shina. “Optimization of LPCVD-SiNx Membranes for Micro-hotplate/Nanoreactors.” MA thesis. Delft University of Technology, 2018.

[20] url: https://app.knovel.com/web/index.v.

[21] Sofia Tönnberg. “Optimisation and characterisation of LPCVD silicon nitride thin film growth.” In: (2006).

[22] A. Khandekar, J. Hull, and S. Joshi. “Low Pressure Chemical Vapor Deposition of Ultra-Thin, Pinhole-Free Amorphous Silicon Films.” In: 2009 IEEE Workshop on Microelectronics and Electron Devices. 2009, pp. 1–4. doi: 10.1109/WMED.2009.4816139.

[23] H. H. Pérez-Garza et al. “The x201C;Climate x201D; system: Nano-Reactor for in-situ analysis of solid-gas interactions inside the TEM.” In: 2016 IEEE 11th Annual International Conference on Nano/Micro Engineered and Molecular Systems (NEMS). 2016, pp. 85–90. doi: 10.1109/NEMS.2016.7758206.

[24] Richard W. Johnson, Adam Hultqvist, and Stacey F. Bent. “A brief review of atomic layer deposition: from fundamentals to applications.” In: Materials Today 17.5 (2014), pp. 236 –246. issn: 1369-7021. doi: https://doi.org/10.1016/j.mattod.2014.04.026. url: http://www.sciencedirect.com/science/article/pii/S1369702114001436.

[25] Ville Miikkulainen et al. “Crystallinity of inorganic films grown by atomic layer deposition: Overview and general trends.” In: Journal of Applied Physics 113.2 (2013), p. 021301. doi: 10.1063/1.4757907. eprint: https://doi.org/10.1063/1.4757907. url: https://doi.org/10.1063/1.4757907.

[26] S. M. George, A. W. Ott, and J. W. Klaus. “Surface Chemistry for Atomic Layer Growth.” In: The Journal of Physical Chemistry 100.31 (1996), pp. 13121–13131. doi: 10.1021/jp9536763. eprint: https://doi.org/10.1021/jp9536763. url: https://doi.org/10.1021/jp9536763.

[27] Ofer Sneh et al. “Thin film atomic layer deposition equipment for semiconductor processing.” In: Thin Solid Films 402.1 (2002), pp. 248 –261. issn: 0040-6090. doi: 10.1016/S0040-6090(01)01678-9. url: https://www.sciencedirect.com/science/article/pii/S0040609001016789.

[28] J. D. Madeley and R. C. Richmond. “A procedure for determining the concentration of Hydroxyl Groups on Silica Surfaces.” In: Zeitschrift für anorganische und allgemeine Chemie 389.1 (1972), pp. 92–96. issn: 1521-3749. doi: 10.1002/zaac.19723890112. url: http://dx.doi.org/10.1002/zaac.19723890112.

[29] L. T. Zhuravlev. “Concentration of hydroxyl groups on the surface of amorphous silicas.” In: Langmuir 3.3 (1987), pp. 316–318. doi: 10.1021/la00075a004. eprint: https://doi.org/10.1021/la00075a004. url: https://doi.org/10.1021/la00075a004.

[30] V Prodanović et al. “Ultra-thin alumina and silicon nitride MEMS fabricated membranes for the electron multiplication.” In: Nanotechnology 29.15 (2018), p. 155703. url: http://stacks.iop.org/0957-4484/29/i=15/a=155703.

[31] JM Rafi et al. “Deposition temperature and thermal annealing effects on the electrical characteristics of atomic layer deposited Al2O3 films on silicon.” In: Journal of The Electrochemical Society 158.5 (2011), G108–G114.

[32] MD Groner et al. “Low-temperature Al2O3 atomic layer deposition.” In: Chemistry of Materials 16.4 (2004), pp. 639–645.

[33] Polarized Light. url: https://www.jawoollam.com/resources/ellipsometry-tutorial/polarized-light.

[34] M. Morita et al. “Growth of native oxide on a silicon surface.” In: Journal of Applied Physics 68.3 (1990), pp. 1272–1281. doi: 10.1063/1.347181. eprint: https://doi.org/10.1063/1.347181. url: https://doi.org/10.1063/1.347181.

[35] JL Van Hemmen et al. “Plasma and Thermal ALD of Al2O3 in a Commercial 200 mm ALD Reactor.” In: Journal of The Electrochemical Society 154.7 (2007), G165–G169.

[36] Alan J Elliot et al. “Probing the Nucleation of Al_2O_3 in Atomic Layer Deposition on Aluminum for Ultrathin Tunneling Barriers in Josephson Junctions.” In: IEEE Transactions on Applied Superconductivity 23.3 (2013), pp. 1101405–1101405.

[37] RRL De Oliveira et al. “Measurement of the nanoscale roughness by atomic force microscopy: basic principles and applications.” In: Atomic Force Microscopy-Imaging, Measuring and Manipulating Surfaces at the Atomic Scale. InTech, 2012.

[38] Cinzia Silvestri. “Carbon Nanotube Based Solutions for On-chip Thermal Management.” PhD thesis. 2017, 21–22.

[39] Tobias Süss, Philipp Braeuninger-Weimer, and Christofer Hierold. “Stress reduction in ultra-small thin film Al2O3 diaphragms by atomic layer deposition.” In: Sensors and Actuators A: Physical 212 (2014), pp. 159 –164. issn: 0924-4247. doi: https://doi.org/10.1016/j.sna.2014.02.021. url: http://www.sciencedirect.com/science/article/pii/S0924424714000855.

[40] Oili M.e. Ylivaara et al. “Aluminum oxide from trimethylaluminum and water by atomic layer deposition: The temperature dependence of residual stress, elastic modulus, hardness and adhesion.” In: Thin Solid Films 552 (2014), 124–135. doi: 10.1016/j.tsf.2013.11.112.

[41] Tobias Süss, Philipp Braeuninger-Weimer, and Christofer Hierold. “Stress reduction in ultra-small thin film Al2O3 diaphragms by atomic layer deposition.” In: Sensors and Actuators A: Physical 212 (2014), pp. 159 –164. issn: 0924-4247. doi: https://doi.org/10.1016/j.sna.2014.02.021. url: http://www.sciencedirect.com/science/article/pii/S0924424714000855.

[42] L. B. Freund and S. Suresh. Thin film materials: stress, defect formation, and surface evolution. Cambridge University Press, 2009.

[43] Dr. Nathan W. Cheung. Lecture notes in Micro-Electro-Mechanical Systems (MEMS) Fabrication. 2010.

[44] K. Kerman et al. “Elastic configurations of self-supported oxide membranes for fuel cells.” In: Journal of Power Sources 222 (2013), pp. 359 –366. issn: 0378-7753. doi: https://doi.org/10.1016/j.jpowsour.2012.08.092. url: http://www.sciencedirect.com/science/article/pii/S0378775312014036.

[45] John W Hutchinson. “Stresses and failure modes in thin films and multilayers.” In: (1996).

[46] Thin Films. url: https://www.psi.ch/lmx-interfaces/thin-films-methods.

[47] X. Feng, Y. Huang, and A. J. Rosakis. “On the stoney formula for a thin film/-substrate system with nonuniform substrate thickness.” In: Journal of Applied Mechanics, Transactions ASME 74.6 (Nov. 2007), pp. 1276–1281. issn: 0021-8936. doi: 10.1115/1.2745392.

[48] Alam Waqi Donaldson Erle C. Gulf Publishing Company, 2008. isbn: 978-1-933762-29-6. url: https://app.knovel.com/hotlink/toc/id:kpW0000001/wettability/wettability.

[49] Thomas W Hansen et al. “Sintering of catalytic nanoparticles: particle migration or Ostwald ripening?” In: Accounts of chemical research 46.8 (2013), pp. 1720–1730.

[50] E. Ruckenstein and S.H. Lee. “Redispersion and migration of Ni supported on alumina.” In: Journal of Catalysis 86.2 (1984), pp. 457 –464. issn: 0021-9517. doi: https://doi.org/10.1016/0021-9517(84)90395-6. url: http://www.sciencedirect.com/science/article/pii/0021951784903956.

[51] D. G. Howitt et al. “The electron beam hole drilling of silicon nitride thin films.” In: Journal of Applied Physics 103.2 (2008), p. 024310. doi: 10.1063/1.2828157. eprint: https://doi.org/10.1063/1.2828157. url: https://doi.org/10.1063/1.2828157.

[52] Patricia Jane Kooyman. “Development of Operando Transmission Electron Microscopy.” In: Operando Research in Heterogeneous Catalysis. Ed. by Joost Frenken and Irene Groot. Cham: Springer International Publishing, 2017, pp. 111–129. isbn: 978-3-319-44439-0. doi: 10.1007/978-3-319-44439-0_5. url: https://doi.org/10.1007/978-3-319-44439-0_5.

[53] Kirt R Williams, Kishan Gupta, and Matthew Wasilik. “Etch rates for micromachining processing-Part II.” In: Journal of microelectromechanical systems 12.6 (2003), pp. 761–778.

[54] K. Shimaoka, H. Funabashi, and Y. Mitsushima. “Characteristics of Silicon Nitride Reaction to Vapor-phase HF Gas Treatment.” In: IEEJ Transactions on Sensors and Micromachines 126 (2006), pp. 516–521. doi: 10.1541/ieejsmas.126.516.

[55] Juan Valle, Daniel Fernandez, and Jordi Madrenas. “Experimental Analysis of Vapor HF Etch Rate and Its Wafer Level Uniformity on a CMOS-MEMS Process.” In: Journal of Microelectromechanical Systems 25.2 (2016), 401–412. doi: 10.1109/jmems.2016.2533267. url: http://ieeexplore.ieee.org/stamp/stamp.jsp?arnumber=7426346.

[56] Piet De Moor Agnes Verbist Chris A. Van Hoof Hugo Bender Christiaan Baert Ann Witvrouw Bert Du Bois. “Comparison between wet HF etching and vapor HF etching for sacrificial oxide removal.” In: vol. 4174. 2000, pp. 4174 –4174 –12. doi: 10.1117/12.396423. url: https://doi.org/10.1117/12.396423.

[57] url: http://www.spts.com/tech-insights/mems/hf-intro.

[58] N. S. Tabrizi et al. “Generation of nanoparticles by spark discharge.” In: Journal of Nanoparticle Research 11.2 (2008), p. 315. issn: 1572-896X. doi: 10.1007/s11051-008-9407-y. url: https://doi.org/10.1007/s11051-008-9407-y.

[59] Ludwig Reimer. Scanning electron microscopy: physics of image formation and microanalysis. Springer, 2010.